

MPX_3 van der Waals magnets under pressure ($M = \text{Mn, Ni, V, Fe, Co, Cd}$; $X = \text{S, Se}$)

Takahiro Matsuoka^{1,2,*}, Heung-Sik Kim^{3,*}, Subhasis Samanta³, Janice L. Musfeldt^{4,*}, David Mandrus^{1,5,*}

¹Department of Materials Science and Engineering, University of Tennessee, Knoxville, Tennessee, USA

²National Institute of Physics, College of Science, University of the Philippines Diliman, Quezon, Philippines

³Department of Physics and Institute of Quantum Convergence Technology, Kangwon National University, Chuncheon, Korea

⁴Department of Chemistry, University of Tennessee, Knoxville, Tennessee, USA.

⁵Materials Science and Technology Division, Oak Ridge National Laboratory, Oak Ridge, Tennessee, USA

Correspondence*:

tatsuoka@up.edu.ph; heungsikim@kangwon.ac.kr; musfeldt@utk.edu; dmandrus@utk.edu

2 ABSTRACT

van der Waals antiferromagnets with chemical formula MPX_3 ($M = \text{V, Mn, Fe, Co, Ni, Cd}$; $X = \text{S, Se}$) are superb platforms for exploring the fundamental properties of complex chalcogenides, revealing their structure-property relations, and unraveling the physics of confinement. Pressure is extremely effective as an external stimulus, able to tune properties and drive new states of matter. In this review, we summarize experimental and theoretical progress to date with special emphasis on the structural, magnetic, and optical properties of the MPX_3 family of materials. Under compression, these compounds host inter-layer sliding and insulator-to-metal transitions accompanied by dramatic volume reduction and spin state collapse, piezochromism, possible polar metal and orbital Mott phases, as well as superconductivity. Some responses are already providing the basis for spintronic, magneto-optic, and thermoelectric devices. We propose that strain may drive similar functionality in these materials.

Keywords: van der Waals solids, complex chalcogenides, external stimuli, compression

1 INTRODUCTION

Transition metal phosphorous trichalcogenides, MPX_3 , where M represents a transition metal ion, and X is either S or Se, are a family of semiconducting van der Waals magnets that were originally discovered in 1894 (Friedel, 1894), but were not studied intensively until the 1970s (Klingen et al., 1973). Originally, interest in these materials was sparked by their low dimensional magnetic properties (Le Flem et al., 1982) and ability to form intercalation compounds (JOHNSON and Jacobson, 1982), but more recently these materials have attracted attention as single-layer magnets (Burch et al., 2018) and as highly tunable systems that undergo bandwidth-controlled Mott transitions under applied pressure (Kim et al., 2019).

22 MPX_3 materials typically crystallize in two space groups, $C2/m$ (No. 12) for the sulfur analogs and $R\bar{3}$
23 (No. 148) for the selenium-containing compounds. In both cases, the M ions form a honeycomb net, and
24 at the center of each hexagon there is a P-P dimer that extends perpendicular to the net. S or Se anions
25 terminate each MPX_3 layer on both sides, and there is a van der Waals gap between the layers, leading to
26 small cleavage energies and easy exfoliability. Single layers of the MPS_3 and MPS_3Se_3 materials can also be
27 viewed as a honeycomb net of M^{2+} ions coordinated by distorted octahedra of S/Se anions, and P-P dimers
28 centering the hexagons and forming a $[P_2S_6]^{-4}$ anionic sublattice. To emphasize the importance of the
29 P-P dimers, the chemical formula of MPX_3 materials is sometimes written as $M_2P_2X_6$, but this is incorrect
30 nomenclature as the chemical formula is not supposed to reflect structural features (Hiroi, 2008). These
31 structural motifs lead to three different types of chemical bonding: ionic, covalent, and van der Waals -
32 which makes understanding the electronic structure of this family of materials quite challenging (Dedkov
33 et al., 2023).

34 In general, MPS_3 materials with $M = V, Mn, Fe, Co,$ and Ni are reported to be antiferromagnetic Mott
35 insulators with variable semiconducting energy gaps and magnetic structures. $CdPS_3$, in contrast, has a
36 filled d shell and is semiconducting and nonmagnetic. The Mottness and magnetism of MPS_3 compounds
37 originates from their partially-filled d -orbital shells; this, in addition to the presence of a van der Waals gap,
38 suggests that the MPS_3 series is an excellent platform for the study of two-dimensional correlated electron
39 phenomena and magnetism.

40 Tuning the physical properties of these compounds is a highly contemporary research subject, allowing
41 for the exploration of new states of matter and functionalities. Toward this end, researchers are using
42 chemical substitution, doping and intercalation, as well as various external perturbations such as electric
43 field, light, strong magnetic fields, and strain (Wang et al., 2018a; Pei et al., 2022). For instance, chemical
44 substitution on the M and X sites provides a viable means to control d -orbital filling and bandwidth,
45 respectively, which are both important parameters to control Mottness, magnetism, and spin-orbital-lattice
46 coupling. Even better, many of MPS_3 compounds have both $X = S$ and $X = Se$ limits as stable systems,
47 which allows continuous tuning of lattice parameter and bandwidth via synthesizing MPS_xSe_{3-x} samples
48 (Basnet et al., 2022b). Even differences in X -site chemistry sometimes gives rise to interesting contrast; for
49 example, the presence and absence of superconductivity in pressurized $FePSe_3$ and $FePS_3$, respectively. At
50 the same time, doping and intercalation control carrier concentration and impart new properties (Basnet
51 et al., 2022a; Tezze et al., 2022).

52 Among these external stimuli, pressure is a highly effective tool for tuning the physical properties of
53 MPX_3 materials. The interlayer van der Waals (vdW) interaction is weak; thus, the interlayer spacing can
54 be effectively modulated by pressure. As the layers are forced closer together, layers slide with respect to
55 each other, changing their relative orientation. Furthermore, pressure modifies the c/a ratio, reflecting the
56 more compressible interlayer distance than the $a-b$ plane. Bond lengths and angles within the chalcogenide
57 layers are also modified under compression.

58 With the collapse of the van der Waals gap upon pressure, interlayer orbital overlap increases, and the
59 materials become more three-dimensional with enhanced bandwidth. Hence, pressure becomes a tuning
60 knob to control both the crossover from two-dimensional to three-dimensional regimes in addition to a
61 bandwidth-controlled Mott transition. With varying d -orbital occupancies and the resulting different orbital
62 degrees of freedoms (i.e. t_{2g} vs. e_g), pressure can induce drastically different responses of lattice structure,
63 as well as electronic and magnetic properties depending on the chemistry of the metal center and chalcogen
64 anion.

65 Secondly, in addition to bandwidth and dimensionality tuning, pressure provides another path to tweak
66 materials properties via ‘layer sliding’ in the MPX_3 compounds (and in other layered vdW systems).
67 Because of the monoclinic structure of many MPS_3 compounds, even hydrostatic pressure can create
68 shear strain that induces sliding of adjacent layers and variation of stacking order. Differences in layer
69 stacking can create contrasting responses in electronic and magnetic properties, as recently suggested in
70 1T-TaS₂ with the “star of David” charge density wave formation. (Butler et al., 2020) The presence of
71 this layer-sliding in the MPS_3 series under pressure, as we will see below, creates complicated yet rich
72 structural, electronic, and magnetic behaviors. Therefore, pressure becomes a valuable tool in unlocking
73 tremendously rich physical characteristics hidden within the MPX_3 series.

74 Over the past few years the evolution of the structural, magnetic, and electronic properties of MPX_3
75 compounds under compression have been extensively studied. Given the rapid progress in this field, the
76 time is ripe for a short review.

77 In the sections below, we first discuss Mn, Fe, and Ni MPX_3 materials, which have been the topics of
78 the most number of studies. We then discuss $V_{0.9}PS_3$ and $CoPS_3$, which have been much less studied.
79 Lastly, we discuss the non-magnetic compounds, $CdPS_3$ and $CdPSe_3$, and the structure-property relations
80 that can be unraveled in these systems. The final section of the review contains future perspectives on this
81 fascinating family of materials.

2 PROPERTIES OF MPX_3 MATERIALS UNDER PRESSURE

82 2.1 $MnPS_3$ and $MnPSe_3$

83 $MnPS_3$ is the prototype in this family of materials and is therefore extensively investigated. This system
84 crystallizes in a monoclinic $C2/m$ structure whereas $MnPSe_3$ displays a trigonal $R\bar{3}$ arrangement. The
85 P–P dimer is an important structural building block as is the $P_2S_6^{4-}$ cluster. These elements are crucial
86 in defining the thickness of the chalcogen layer. Table 1 summarizes the layer thickness and van der
87 Waals gap for $MnPS_3$ and $MnPSe_3$ and compares them to other members of this series. The $C2/m$ vs. $R\bar{3}$
88 structural difference between sulfur and selenium analogs plays out in other members of the MPX_3 family
89 of materials as well [Fig. 1 + Tables 2 and 3].

90 Early neutron diffraction studies of $MnPS_3$ uncovered collinear Néel-type AFM order at $T_N = 78$ K, (Le
91 Flem et al., 1982; Kurosawa et al., 1983b; Joy and Vasudevan, 1992; Wildes et al., 1994) although there were
92 discrepancies as to the direction of the magnetic propagation vector. A recent study revisited this problem
93 using single crystal neutron diffraction and polarimetry. (Ressouche et al., 2010) This work revealed
94 a propagation vector $\mathbf{k} = [000]$ as well as magnetoelectric coupling and ferrotoroidicity. (Ressouche
95 et al., 2010) By comparison, $T_N = 74$ K for $MnPSe_3$. (Wiedenmann et al., 1981; Le Flem et al., 1982)
96 A similar reduction of the transition temperature is observed for $FePX_3$ when the X is modified from
97 sulfur to selenium. Neutron scattering of $MnPSe_3$ reveals an identical propagation vector ($\mathbf{k} = [000]$).
98 (Wiedenmann et al., 1981; Bhutani et al., 2020) Photoemission and x-ray absorption spectroscopy confirms
99 a high spin Mn^{2+} configuration in $MnPSe_3$. (Fujii et al., 2022) Each Mn center is antiferromagnetically
100 coupled to its three nearest neighbors. (Kurosawa et al., 1983a) One surprising finding is the strong
101 magnetic interaction between third nearest neighbors. The spin wave excitations have also been studied by
102 Raman and neutron scattering in these materials. Major findings include: hybridization of the two-magnon
103 excitation with phonons (which impacts the spin wave decoherence pathway) and absence of nonreciprocity
104 in zone boundary magnons (which provides experimental limits that can be tested against theoretical
105 predictions). (Sun et al., 2019; Vaclavkova et al., 2020; Mai et al., 2021; Wildes et al., 2021)

106 Several different but complementary efforts were required to unravel the sequence of events that takes
107 place under pressure. In the first experimental work, Wang *et al.* uncovered a simultaneous spin-state
108 crossover and metal-insulator transition in both MnPS₃ and MnPSe₃ [Fig. 2] as well as zigzag chain
109 formation of the Mn atoms in the metallic phase. (Wang *et al.*, 2016) The critical pressures (P_c 's) for
110 these processes were reported to be 30 and 25 GPa for MnPS₃ and MnPSe₃, respectively. First-principles
111 electronic structure calculations using DFT + U and DFT + DMFT techniques reproduced the insulator-
112 to-metal transition with simultaneous spin-state transition but with a Mn-Mn dimerization at 64 GPa,
113 (Kim *et al.*, 2019) although it was hinted that some structural components might be missing. This early
114 experimental and theoretical work did not consider layer sliding, which turns out to modify the picture in
115 important ways.

116 In a significant conceptual advance, Coak *et al.* discovered an intermediate pressure transition in the
117 series of MPS₃ ($M = V_{0.9}$, Mn, Fe, Ni) materials. (Coak *et al.*, 2020) This transition involves coherent
118 layer sliding to create an alignment of P–P dimers along the layer-normal direction. This insight enabled a
119 number of subsequent advancements. For instance, infrared, Raman scattering, and optical measurements as
120 a function of pressure combined with first-principles calculations reveal that MnPS₃ undergoes a $C2/m$ (LP)
121 $\rightarrow P\bar{3}1m$ (HP-I, insulating, around 10 GPa) $\rightarrow C2/m$ (HP-II, metallic, around 30 GPa) with a layer-sliding
122 between the LP and HP-I phases, similar to observed in FePS₃ [Fig. 1 and Table 2]. The HP-I to HP-II
123 transition accompanies spin-state transition, collapse of MnS₆ volume, and a sudden collapse of interlayer
124 distance with an layer-normal P-chain formation, consistent to observations reported in FePS₃ [Figs. 1,
125 2, and 3]. The trigonal-to-monoclinic symmetry lowering at the HP-I \rightarrow HP-II transition is thought to
126 originate from the low-spin d^5 orbital nature of the Mn²⁺ ions, contrary to the case of FePS₃ with the
127 same layer sliding but with $C2/m$ (LP) $\rightarrow C2/m$ (HP-I, insulating after the layer sliding) $\rightarrow P\bar{3}1m$ (HP-II,
128 metallic) transitions.

129 We note in passing that theory tends to over-estimate the band gap and pressure of the insulator-to-metal
130 transition in these materials. (Grasso *et al.*, 1991; Harms *et al.*, 2020; Yan *et al.*, 2023) Gap estimation is a
131 well-known challenge for first-principles density functional theory-based approaches, and weak interactions
132 with shallow potentials are notoriously difficult to calculate with accuracy. Nevertheless, these techniques
133 nicely reveal the semiconducting behavior of the aligned phosphorous dimer phase and the metallic
134 character of the aligned phosphorous chain phase [Fig. 4].

135 From the optical properties point of view, MnPS₃ is a semiconductor with a 2.7 eV band gap. It hosts
136 spin-charge coupling across the magnetic ordering transition and a set of crystal field excitations that have
137 been widely investigated. (Boerio-Goates *et al.*, 1981; Grasso *et al.*, 1991; Harms *et al.*, 2020; Yan *et al.*,
138 2023; Park *et al.*, 2024) There is strong p - d hybridization which activates the d -to- d on-site excitations of
139 the Mn²⁺ centers. There is also a broad near infrared emission band assigned as $^4T_1 \rightarrow ^6A_1$ with a half life
140 of approximately 50 μ sec at 77 K. (Boerio-Goates *et al.*, 1981) The ratio of the crystal field splitting to the
141 Racah parameter ($10Dq/B$) is unusually large and may explain the strongly red-shifted light emission in
142 this system. That the band gap of MnPS₃ decreases systematically under pressure suggests that this system
143 hosts piezochromism. (Harms *et al.*, 2020) It turns out that MnPS₃ is green at ambient conditions, and as
144 shown in Fig. 5, it is yellowish-green at 3 GPa, bright red at 8 GPa, and black by 20 GPa. The latter occurs
145 because the band gap shifts out of the visible wavelength range, moving systematically toward closure at
146 a rate of approximately -50 meV/GPa. This effect is quenched by the appearance of the insulator–metal
147 transition. This high level of linear responsivity under pressure is unusual, and piezochromism of this
148 type has applications in pressure sensing, actuation, as well as artificial skin. At this time, it is not known
149 whether strain can drive similar effects in the bulk material, although in few- and single-sheet MnPS₃ there

150 is a $C2/m$ to $P\bar{3}1m$ transition that may involve surface strain effects (Neal *et al.*, 2019, 2020) and biaxial
151 strain is predicted to impact the magnetic ground state in $MnPS_3$ monolayers.(Pei *et al.*, 2018)

152 Thermal properties of these materials are also of interest from a fundamental point of view and for heat
153 management purposes in a device. Kargar *et al.* find in- and out-of-plane thermal conductivities of $6.3 \pm$
154 1.7 and 1.1 ± 0.2 W/m·K, respectively.(Kargar *et al.*, 2019) These values are higher than what is found in
155 the Fe analog.

156 2.2 FePS₃ and FePSe₃

157 FePS₃ and FePSe₃ have been reported as layered antiferromagnets with T_N s around 120 K. (Le Flem
158 *et al.*, 1982; Joy and Vasudevan, 1992). FePS₃ has gained significant interest recently for its Ising-like
159 antiferromagnetic ordering in the single-layer limit. (Lee *et al.*, 2016) The d^6 configuration of the Fe^{2+}
160 charge status shows a high-spin configuration $S = 2$ with the partially-filled t_{2g} complex, implying
161 anisotropic nature of magnetism as revealed by experimental and theoretical observations. (Nauman *et al.*,
162 2021; Zhang *et al.*, 2021) In the presence of external pressure, like Mn-based siblings, spin-state transition
163 and the resulting complex electronic and structural responses are expected in FePS₃ and isostructural
164 FePSe₃. Accordingly, the responses of magnetic, electronic, and structural properties of FePS₃ and FePSe₃
165 have been actively investigated.

166 Recent x-ray, neutron scattering, and optical spectroscopy studies on the effect of hydrostatic pressure on
167 FePS₃ reveal a sequence of structural phase transition, (Haines *et al.*, 2018; Coak *et al.*, 2021; Harms *et al.*,
168 2022b) analogous to $MnPS_3$ and $V_{1-x}PS_3$ (Harms *et al.*, 2020; Coak *et al.*, 2019); a gradual layer-sliding
169 crossover from the monoclinic ambient ($C2/m$ space group) to the pseudo-hexagonal intermediate phase
170 (HP-I, $C2/m$) around 2~5 GPa, and the following $C2/m \rightarrow P\bar{3}1m$ (HP-II) transition accompanied by the
171 insulator-to-metal transition at 14 GPa (see Fig. 1). (Coak *et al.*, 2021) The ambient and HP-I phases
172 of FePS₃ have been reported to be insulating and antiferromagnetic with a Néel-type order. Figures 6a
173 and b show the magnetic configurations of the ambient and HP-I phases from neutron data, respectively.
174 (Coak *et al.*, 2021). Figure 6c describes the evolution of the T_N as a function of pressure. (Wang *et al.*,
175 2018b; Haines *et al.*, 2018; Coak *et al.*, 2021) The gradual enhancement of the T_N can be attributed to
176 the increased kinetic energy scale due to the closer Fe-Fe distances and the resulting enhanced magnetic
177 exchange interactions.

178 The second transition (HP-I \rightarrow HP-II) accompanies the breaking of the P-P dimer structure and the
179 formation of interlayer P-chain perpendicular to the Fe layers, in addition to a sudden collapse of the
180 interlayer distance and volume, (Haines *et al.*, 2018) similar to the case of $MnPS_3$. (Harms *et al.*, 2020)
181 Note that these observations are consistent with separate first-principles electronic structure calculation
182 results, (Zheng *et al.*, 2019; Deng *et al.*, 2023) where the origin of the coexistence of the ambient and
183 HP-I phases around 2~5 GPa is suggested to be the result of the shear-induced energy barrier between the
184 ambient and HP-I phases (see Fig. 7a). (Deng *et al.*, 2023)

185 From both experimental and theoretical studies the Mott-insulating antiferromagnetic phase is reported
186 to remain robust in the ambient and HP-I phases, reflecting the quasi-two-dimensional nature. Haines
187 *et al.* (2018); Zheng *et al.* (2019) With the formation of the interlayer P-chain in the HP-II phase this
188 two-dimensional character breaks down, and so does the insulating behavior. The sudden collapse of the
189 interlayer distance and cell volume at the HP-I \rightarrow II transition implies a spin-state transition (see Fig. 3).
190 Indeed, an early study on pressurized phases of FePS₃ and FePSe₃ reported collapses of magnetic moments
191 and transitions to low-spin phases around 13 and 8 GPa, respectively, Wang *et al.* (2018b) and additionally,
192 the DFT study of Zheng *et al.* also reports the spin-state transition from the high-spin $S = 2$ to the low-spin

193 $S = 0$ configuration of the Fe ions at the HP-I→II transition. (Zheng *et al.*, 2019) Interestingly, on the
194 other hand, a high-pressure neutron diffraction data by Coak *et al.* suggests the presence of short-range
195 magnetic order in the HP-II phase, persisting even up to room temperature (see Fig. 6c). Coak *et al.* (2021)
196 From a detailed electronic structure calculation study, Deng *et al.* argues that this puzzling behavior may
197 be explained by the potential coexistence of two metastable metallic states; the high-spin one with the
198 intra-layer P_2 dimer structure remains intact comparing the short-range order(2D-like), while the P_2 dimer
199 breaks to form the out-of-plane P chain structure (3D-like) in the other low-spin state. (Deng *et al.*, 2023)
200 A separate dynamical mean-field theory study on FePS₃ also suggests the coexistence of the two structural
201 phases, each one hosting the normal Fermi liquid-like character (with the interlayer P-chain) and the
202 incoherent ‘Hund’s metal’ character (with the intralayer P-dimer) in the high-pressure regime, where the
203 Hund’s metal phase keeps the local moments intact and induces bad-metallic behavior due to magnetic
204 fluctuations. (Kim *et al.*, 2022)

205 It is interesting to note that, in Kim *et al.*, the Hund’s metal phase with the orbital-selective correlation
206 effects occurs only with a non-hydrostatic pressure, especially when the pressure perpendicular to the
207 Fe layers are stronger than the in-plane counterparts. This originates from the direction-selective orbital
208 effect under pressure, where the t_{2g} orbitals of Fe ions becomes more susceptible to the out-of-plane
209 stress compared to e_g . (Kim *et al.*, 2022) This implies a subtle role of anisotropy and inhomogeneity in
210 pressure, which may often occur in high-pressure experimental situations depending on the choices of
211 pressure-transmitting medium. (Matsuoka *et al.*, 2021).

212 Lastly we comment on FePSe₃. This system shares a crystal structure and magnetic ground state with
213 FePS₃, (Le Flem *et al.*, 1982; Wiedenmann *et al.*, 1981) and expected from theoretical calculations to
214 show many common properties, such as layer-sliding transition to HP-I, volume collapse at the HP-I→II
215 transition accompanying the simultaneous spin-state and insulator-metal transitions. (Zheng *et al.*, 2019)
216 Experimentally the second transition is observed to occur at a lower pressure of around 8 GPa than that
217 of FePS₃, which can be attributed to the larger hybridization effects from Se ions. (Wang *et al.*, 2018b)
218 Unlike FePS₃, superconductivity of unknown origin has been reported in the HP-II metallic phase of
219 FePSe₃ below 2.5K (see Fig. 7c and d). (Wang *et al.*, 2018b) Structural refinement in the same study
220 suggests the formation of the zigzag chains within the Fe honeycomb layer in the HP-II phase of FePSe₃,
221 hinting the presence of orbital physics from high-spin configuration at Fe ions and potential unconventional
222 superconductivity.

223 2.3 NiPS₃ and NiPSe₃

224 NiPS₃ and the Se analog provide another exciting platform for exploring new states of matter under
225 external stimuli and developing different types of structure-property relationships. The magnetic ordering
226 temperatures are $T_N = 155$ and 206 K, respectively (Le Flem *et al.*, 1982; Joy and Vasudevan, 1992;
227 Chandrasekharan and Vasudevan, 1994), so we see that in this case, heavier anions act to raise the
228 Néel temperature. In the low temperature phase of NiPS₃, the magnetic propagation vector $\mathbf{k} = [010]$.
229 Analysis of the integrated intensity of the (010) magnetic Bragg peak as a function of temperature reveals a
230 critical exponent for the magnetization $2\beta = 0.30$ away from the transition temperature, consistent with
231 a two-dimensional universality class, and 0.30 near T_N , suggesting the importance of three-dimensional
232 interactions in this regime (Wildes *et al.*, 2015). There are a number of low energy excitations in this system
233 from which competing exchange interactions can be extracted (Wildes *et al.*, 2023; Mehlawat *et al.*, 2022),
234 and active pumping of orbital resonances can also manipulate magnetic order in this quasi-two-dimensional
235 van der Waals antiferromagnet (Afanasyev *et al.*, 2021). Solid solutions in the form of Ni_{1-x}Mn_xPS₃ ($0 \leq$

236 $x \leq 1$) can also tune the spin flop transition from approximately 7 to 2 T due to modulation of the magnetic
237 anisotropy. (Basnet et al., 2021) Intercalation is also very effective in this regard. It can even drive the
238 ground state ferrimagnetic. (Basnet et al., 2022a; Tezze et al., 2022) The magnetic properties of NiPS₃ are
239 clearly very sensitive to chemical pressure, suggesting that there is more to learn under physical pressure.
240 The latter is obviously a much cleaner technique as well. Light is also an important external stimuli in these
241 materials. NiPS₃, for instance, sports laser-induced demagnetization with responsivity (lifetime) on the
242 order of 10 ps. Kuntu et al. (2023) Photo-induced quenching of magnetic order is likely to be very sensitive
243 to pressure.

244 Early high pressure x-ray diffraction work combined with first-principles calculations suggested strong
245 similarities between NiPS₃ and the $M = \text{Mn}$ and V analogs, with LP-to-HP-I and the HP-I-to-HP-II
246 transitions near 15 and 27 GPa with an insulator-to-metal transition near 20 GPa (Ma et al., 2021). More
247 recent efforts combining transport and x-ray diffraction reveal a series of different crystal structures under
248 pressure, time-dependent and somewhat sluggish character to several of the transitions, and an insulator-
249 to-metal transition near 30 GPa. (Matsuoka et al., 2021) Systematic studies of hydrostatic pressure vs.
250 strain demonstrates that the critical pressure of the insulator-to metal transition (as identified by transport
251 measurements) is reduced from 30 to 12.5 GPa under uniaxial strain (Cui et al., 2021) - an observation that
252 again emphasizes the need for hydrostatic pressure conditions. This confusing and somewhat contradictory
253 picture was resolved by bringing together synchrotron-based infrared absorption, Raman scattering, x-ray
254 diffraction, and first-principles calculations under pressure to show that in fact NiPS₃ is quite different from
255 the other MPS₃ materials (Harms et al., 2022a) with a series of five different critical pressures. The set of
256 symmetry progressions in this material is complex (involving $C2/m \rightarrow P\bar{3} \rightarrow P\bar{3}m1 \rightarrow P3m1 \rightarrow P3 \rightarrow P1$
257 space groups) from monoclinic to trigonal to noncentrosymmetric trigonal to triclinic phases (Figs. 8 and
258 9). The insulator-to-metal transition takes place near 23 GPa as evidenced by the development of a Drude
259 response + screening of the phonons in the infrared spectrum. This definition of the insulator-to-metal
260 transition obviously places the critical pressure below that obtained from a transport measurement (23
261 vs. 30 GPa), but the development of Drude signature in the electrodynamic response is an exquisitely
262 sensitive indicator of metallicity. In any case, it's important to realize that several of the aforementioned
263 space groups lack an inversion center, suggesting that NiPS₃ may be a polar metal under compression.
264 (Harms et al., 2022a) Whether the material is switchable (ferroelectric) or not switchable (pyroelectric)
265 under these conditions (in the $P3m1$ phase above 23 GPa) is unexplored at present. In principle, any electric
266 polarization should increase as the space group progresses from $P3m1 \rightarrow P3 \rightarrow P1$. (Harms et al., 2022a;
267 Aoyama et al., 2014) Real physical examples of polar metals are rare, so it's useful to consider how NiPS₃
268 hosts such a state when it has not been sighted (as of yet) in related MPX₃ systems. The current working
269 hypothesis is that because NiPS₃ does not favor a $P\bar{3}m1$ -type structure or layer-normal phosphorous chain
270 formation, it may engage in negative charge transfer with hole formation at the S sites. (Harms et al.,
271 2022a). The optical properties of NiPS₃ have also been of sustained interest (Kim et al., 2018; Kang et al.,
272 2020; Lane and Zhu, 2020) - both in single crystal and thin film form - although to our knowledge, there
273 have been no studies under pressure or strain. Interestingly, electric field also drives an insulator-to-metal
274 transition in the monolayer (Lane and Zhu, 2020), suggesting that pressure and electric field phase space
275 may share more similarities than previously supposed.

276 NiPSe₃ is different, primarily because it does not have a complicated set of symmetry progressions under
277 compression. Instead, there is a relatively simple structural sequence as shown in Fig. 10 and Table 3.
278 (Harms et al., 2022a; Sun et al., 2023) More recent efforts involving combined synchrotron x-ray diffraction
279 and first-principles theory confirm these two structural transitions: LP to HP1 (where the honeycomb
280 layers slide relative to each other) and HP1 to HP2 (where the structure has more three-dimensional

281 character) (Sun *et al.*, 2023). There is also a concomitant magnetic crossover at $P_{C,1}$ where the direction
282 of the antiferromagnetic moment switches from out-of-plane to in-plane. Complementary resistance
283 measurements indicate a bandwidth-controlled Mott insulator-metal transition near 8.0 GPa. The latter
284 coincides with the emergence of superconductivity with $T_c \approx 4.8$ K. (Sun *et al.*, 2023) This leads to a
285 remarkable and complex pressure-temperature phase diagram hosting coexisting zigzag antiferromagnetic
286 order and superconductivity [Fig. 11].

287 Finally, we point out that transition metal dichalcogenides such as MoS₂ and WS₂ and related
288 nanostructures are employed for solid state lubrication due to their ultra-low friction coefficients -
289 especially under high shear conditions. (Musfeldt *et al.*, 2020) In an important initiative, Deng *et al.*
290 are starting to explore the mechanical properties of ternary chalcogenides like NiPS₃ using lateral force
291 microscopy. (Deng *et al.*, Friction, under review, (2024) These measurements reveal a friction coefficient
292 of approximately 4.5×10^{-3} under 5×10^{-3} Pa with load up to 768 nN. These findings are discussed in
293 terms of the extremely weak interlayer interactions. Table 1 summarizes other candidates with low layer
294 thickness/van der Waals gap ratios including CdPS₃ and FePSe₃ that should be tested.

295 2.4 V_{1-x}PS₃ ($x < 1$)

296 The vanadium phosphate synthesis has been achieved with the vanadium deficiency in V_{1-x}PS₃ which
297 can be explained as due to valence mixing on the vanadium site between V²⁺ and V³⁺ states (Ouvrard
298 *et al.*, 1985b; Ichimura and Sano, 1991). The LP-phase has an electrical conductivity higher than 10^{-5}
299 Scm⁻¹, while MnPS₃, NiPS₃ and ZnPS₃ crystals lower than 10^{-9} Scm⁻¹ at room temperature. The high
300 conductivity of the former crystals is attributed to their mixed valency on the metal and/or the S and
301 P sites, which has been revealed by x-ray photoelectron spectroscopy. (Ichimura and Sano, 1991) The
302 LP → HP-I transition starts at 2.6 GPa followed by the gradual transition to HP-I completing near 8.0
303 GPa. (Coak *et al.*, 2019) The layers of V_{0.9}PS₃ shift relative to each other in a sliding motion of $\sim a/3$
304 along the *a*-axis such that the S atoms become arranged in a hexagonal closed packing layout between
305 the layers (Table 2, and Fig.1). (Coak *et al.*, 2019) In HP-I, P atoms are slightly distorted along the *a*-axis
306 (the *x* coordinate value is 0.0074 at 17.7 GPa) of the unit cell, and this distortion results in the same
307 C2/m symmetry. (Coak *et al.*, 2019) The volume per formula unit ($V_{f.u.}$) decreases continuously without a
308 sudden or discontinuous changes across the gradual LP → HP-I transformation (Fig. 3). (Coak *et al.*, 2019)
309 The electrical resistance decreases significantly and continuously with increasing pressure, and then the
310 insulator-to-metal transition occurs near 12 GPa above the pressure where the LP → HP-I transformation
311 completes. (Coak *et al.*, 2019) Thus, the isostructural insulator-to-metal transition is concluded, suggesting
312 a second-order transition. (Coak *et al.*, 2019) From the magnetoresistance data, Coak *et al.* claim the ITM
313 involves the antiferromagnetic to paramagnetic transition. (Coak *et al.*, 2019) The *R* vs. *T* curve in the
314 metallic phase shows an upturn at low temperatures. (Coak *et al.*, 2019) Coak *et al.* suggest that Kondo
315 effect due to the vanadium deficiency and disordered valence mixing on the vanadium sites. (Coak *et al.*,
316 2019) The synthesis of VPS₃ has not been reported to the knowledge of the authors.

317 2.5 CoPS₃ and CoPSe₃

318 Like other structural siblings, CoPS₃ has gained significant interests recently for the study of two-
319 dimensional magnetism. Since Co²⁺ ion is in the *d*⁷ configuration with a hole in the *t*_{2g} shell, significant
320 effects of spin-orbit coupling on magnetism is expected. Indeed, recent theoretical studies suggested an
321 interesting way to realize the so-called Kitaev's exchange interactions in cobalt-based compounds, (Kitaev,
322 2006; Liu and Khaliullin, 2018; Sano *et al.*, 2018) which were originally considered in heavier transition
323 metal systems. (Jackeli and Khaliullin, 2009) Several Co-based systems including CoPS₃ have been studied

324 for the search of the Kitaev-induced frustrated magnetism. (Kim et al., 2020, 2021; Lin et al., 2021; Zhang
325 et al., 2023; Kim et al., 2023) Considering the presence of metastable spin states and significant spin-orbit
326 coupling in Co ions, (Yamaguchi et al., 1996; Zobel et al., 2002) it is expected that pressure may induce
327 intriguing evolution of electronic and magnetic properties of CoPS₃.

328 CoPS₃ crystallizes in *C2/m* structure at ambient pressure as other MPS₃ family at ambient pressure.
329 CoPS₃ exhibits AFM at ambient pressure with a $T_N = 122$ K and a Weiss temperature of $\theta = -166$
330 K. (Ouvrard et al., 1982; Wildes et al., 2017) Single-crystal neutron diffraction shows that the magnetic
331 propagation vector is $\mathbf{k} = [010]$ with the moments mostly along the *a*-axis and with a small component
332 along the *c*-axis. (Ouvrard et al., 1982; Wildes et al., 2017) This magnetic structure is in sharp contrast to
333 MnPS₃ and FePS₃, as observed for NiPS₃. Its effective moment is $4.9 \mu_B$, slightly larger than the expected
334 value for a pure spin moment of a Co²⁺ cation (Ouvrard et al., 1982), implying orbital contribution to the
335 magnetization as mentioned above. In addition, an inelastic neutron scattering study suggests a XXZ-type
336 antiferromagnetic order in CoPS₃, signalling the presence of the spin-orbit coupling-induced magnetic
337 anisotropy. (Kim et al., 2020)

338 High-pressure properties of CoPS₃ have not been experimentally reported until recently, probably
339 due to the significant difficulty in the synthesis and single crystal growth of this compound. A first-
340 principles calculation from an article dedicated to the pressure effects in CoPS₃ predicts a pressure-driven
341 isostructural Mott transition accompanied by a spin crossover. (Gu et al., 2021) XRD and Raman scattering
342 measurements reveal that CoPS₃ exhibits *C2/m* (LP) \rightarrow $P\bar{3}$ (HP-I) structural transformation (Figure 1 and
343 Table 2) at 7 GPa and room temperature accompanied by the small drop (2.9%) of the volume per formula
344 unit (Figure 3). (Matsuoka et al., 2023) This volume collapse and comparing FePS₃ and MnPS₃, it is
345 concluded that CoPS₃ exhibits the spin crossover ($S = 3/2 \rightarrow 1/2$) accompanied by the metallization.
346 On the other hand, the 2.9% of volume collapse is much smaller than that of FePS₃ (10.6%) and MnPS₃
347 (19.7%) (Figure 3 and 3). (Matsuoka et al., 2023; Wang et al., 2016; Haines et al., 2018; Wang et al., 2018b)
348 The ionic radii of high- (HS, 0.89 Å) and low-spin (LS, 0.79 Å) Co²⁺ ions make the HS \rightarrow LS radius
349 reduction 11.2%, which is not much smaller than that of Mn²⁺ (HS: 0.97 Å, LS: 0.81 Å, 16.5%) and Fe²⁺
350 (HS: 0.92 Å, LS: 0.75 Å, 18.5%) (Shannon, 1976). Thus, the slight volume reduction of CoSP₃ cannot
351 be explained solely by the difference between HS and LS radii. It is also noticeable that the volume per
352 formula unit and *c*-axis in the $P\bar{3}$ phase show a steeper compression between 7 GPa and 12 GPa followed
353 by moderate compression above 12 GPa, indicating a sign of structural stabilization. (Matsuoka et al., 2023)
354 These series of changes in compression behavior suggest an electronic transition in the $P\bar{3}$ phase. Upon
355 decompression at room temperature, the $P\bar{3}$ phase remains down to 2 GPa revealing a large hysteresis in
356 the volume per formula unit and *c*-axis. (Matsuoka et al., 2023)

357 Concomitantly with the structural transition, the electrical resistance decreases significantly and CoPS₃
358 becomes metallic. (Matsuoka et al., 2023) The positive Hall resistivity reveals this metallic CoPS₃ is a hole-
359 dominant conductor with multiple conduction bands, and its non-saturating behavior against the external
360 magnetic field, indicating the absence of the anomalous Hall effect, suggests that the metallic CoPS₃ is not
361 ferromagnetic (Figure 12). (Matsuoka et al., 2023) The linear magnetoresistance ($\Delta\rho_{xy}(B)/\rho_{xx}(B = 0)$),
362 where $\Delta\rho_{xx}(B) = \rho_{xx}(B) - \rho_{xx}(B = 0)$), along with the small volume collapse at the metallization,
363 suggest the incomplete high-spin \rightarrow low-spin transition in the metallic phase (Figure 12). (Matsuoka et al.,
364 2023) It is expected that the metallic CoPS₃ possibly possesses an inhomogeneous magnetic moment
365 distribution and short-range magnetic ordering. (Matsuoka et al., 2023) Furthermore, the magnetoresistance
366 changes from linear to more quadratic magnetic field dependent as pressure increases. (Matsuoka et al.,
367 2023) Considering the suggested electronic transition from the volume per formula unit vs. pressure slope
368 across 12 GPa (Figure 3), it can be thought that the spin crossover proceeds with pressure up to 12 GPa and

369 stops or progress moderately above 12 GPa in the $P\bar{3}$ phase (Matsuoka et al., 2023).

370

371 2.6 CdPS₃ and CdPSe₃

372 CdPS₃ crystallizes in the $C2/m$ structure with the monoclinic angle $\beta = 107.27^\circ$, possessing an insulating
373 electrical character like other MPX_3 family members (Ouvrard et al., 1985a; Niu et al., 2022). The Raman
374 scattering measurements combined with *ab-initio* calculation reveal that CdPS₃ exhibits two structural
375 transformations the LP-phase ($C2/m$) \rightarrow HP-I phase ($R\bar{3}$) that initiates near 0.11 GPa and completes near
376 1.1 GPa (Niu et al., 2022). The HP-I ($R\bar{3}$) \rightarrow HP-II ($R\bar{3}$) unedergoes from 7.35 GPa to 10.2 GPa (Niu
377 et al., 2022). The $C2/m \rightarrow R\bar{3}$ transition is obtained by sliding a single layer of the LP-phase along the
378 B axis for a distance of about $\frac{b}{6}$ and simultaneously sliding it for approximately $\frac{a}{3}$ along the a axis. This
379 results in the $C2/m$ unit's β angle changing from 107.27° to approximately 90° (Niu et al., 2022). The HP-I
380 ($R\bar{3}$) to HP-II ($R\bar{3}$) transition is instead caused by the distortion of CdS₆ polyhedrons (Niu et al., 2022).
381 The *ab-initio* calculation suggests a small volume reduction (-2.05%) with the LP-I \rightarrow HP-I transformation
382 (Niu et al., 2022). On the other hand, the volume vs. P curves of HP-I and HP-II almost overlap across
383 a wide pressure range (2 - 22 GPa), reflecting the transformation nature (Niu et al., 2022). The *ab-initio*
384 calculation also suggests the further transformation from HP-II to HP-III ($P\bar{3}1m$) at approximately 25 GPa
385 (Niu et al., 2022). Compared with other MPM_3 , it is noticeable that the LP-phase of CdPS₃ is relatively
386 more sensitive to external pressure than other MPX_3 reported so far (Table 2). This would suggest that even
387 a slight strain can be an effective stimulus to drive the appearance of a new structural phase of CdPS₃.

3 SUMMARY AND FUTURE PROSPECTS

388 Complex chalcogenides display properties and states of matter that are incredibly sensitive to external
389 stimuli. This particular review is inspired by opportunities to employ pressure to unveil elusive states of
390 matter and uncover charge-structure-function relationships. Compression is particularly well-suited to
391 tuning the properties of chalcogenides because, in addition to changing bond lengths and angles, it provides
392 deterministic control of the c/a structural ratio and the van der Waals gap. By controlling the environment
393 around the metal center, compression also controls spin. As emphasized throughout this review, strain is
394 likely to offer complementary advantages. At the same time, expanding the chemical phase space of the
395 MPX_3 system to include solid solutions like (Zn,Cd)PS₃ or (Ni,Co)PS₃, heavy 4- and 5d- metal centers
396 to enhance spin-orbit coupling, the CrPS₄ member of this family, and dual sublattice analogs such as
397 bimetallic CuInP₂S₆ and AgInP₂S₆ provides exciting new platforms for exploring ferroelectricity, new
398 types of photoinduced behavior, ionic motion, and even charge pumping under compression.

CONFLICT OF INTEREST STATEMENT

399 The authors declare that the research was conducted without any commercial or financial relationships that
400 could be construed as a potential conflict of interest.

AUTHOR CONTRIBUTIONS

401 All authors contributed equally to the discussions, reviewing, and writing of this manuscript.

FUNDING

402 JLM thanks Physical Behavior of Materials, Basic Energy Sciences, U.S. Department of Energy
403 (Contract number DE-SC00023144) for support of this work. HSK and SS are supported by the Korea
404 Research Fellow (KRF) Program and the Basic Science Research Program through the National Research
405 Foundation of Korea funded by the Ministry of Education [Grant No. NRF-2019H1D3A1A01102984,
406 NRF-2020R1C1C1005900, and RS-2023-00220471]. DM is funded by the Gordon and Betty Moore
407 Foundation's EPiQS Initiative, Grant No. GBMF9069. TM thanks the support by the Air Force Office of
408 Scientific Research under award number FA2386-23-1-4112.

REFERENCES

- 409 Afanasiev, D., Hortensius, J. R., Matthiesen, M., Mañas-Valero, S., Šiškins, M., Lee, M., et al. (2021).
410 Controlling the anisotropy of a van der Waals antiferromagnet with light. *Science Advances* 7, eabf3096.
411 doi:10.1126/sciadv.abf3096
- 412 Aoyama, T., Yamauchi, K., Iyama, A., Picozzi, S., Shimizu, K., and Kimura, T. (2014). Giant spin-
413 driven ferroelectric polarization in TbMnO₃ under high pressure. *Nature Communications* 5, 4927.
414 doi:10.1038/ncomms5927
- 415 Basnet, R., Ford, D., TenBarge, K., Lochala, J., and Hu, J. (2022a). Emergence of ferrimagnetism in
416 Li-intercalated NiPS₃. *Journal of Physics: Condensed Matter* 34, 434002. doi:10.1088/1361-648X/
417 ac8a81
- 418 Basnet, R., Kotur, K. M., Rybak, M., Stephenson, C., Bishop, S., Autieri, C., et al. (2022b). Controlling
419 magnetic exchange and anisotropy by nonmagnetic ligand substitution in layered m p x 3 (m= ni, mn;
420 x= s, se). *Physical Review Research* 4, 023256
- 421 Basnet, R., Wegner, A., Pandey, K., Stormont, S., and Hu, J. (2021). Highly sensitive spin-flop transition in
422 antiferromagnetic van der Waals material MPS₃ (M = Ni and Mn). *Physical Review Materials* 5, 064413.
423 doi:10.1103/PhysRevMaterials.5.064413
- 424 Bhutani, A., Zuo, J. L., McAuliffe, R. D., dela Cruz, C. R., and Shoemaker, D. P. (2020). Strong
425 anisotropy in the mixed antiferromagnetic system Mn_{1-x}Fe_xPSe₃. *Physical Review Materials* 4,
426 034411. doi:10.1103/PhysRevMaterials.4.034411
- 427 Boerio-Goates, J., Lifshitz, E., and Francis, A. H. (1981). Electronic spectroscopy of nearly octahedrally
428 coordinated manganese in manganese phosphide sulfide (MnPS₃) and cadmium phosphide sulfide
429 (CdPS₃) lattices. *Inorganic Chemistry* 20, 3019–3023. doi:10.1021/ic50223a052
- 430 Burch, K. S., Mandrus, D., and Park, J.-G. (2018). Magnetism in two-dimensional van der waals materials.
431 *Nature* 563, 47–52
- 432 Butler, C., Yoshida, M., Hanaguri, T., and Iwasa, Y. (2020). Mottness versus unit-cell doubling as the
433 driver of the insulating state in 1 t-tas2. *Nature communications* 11, 2477
- 434 Chandrasekharan, N. and Vasudevan, S. (1994). Magnetism and exchange in the layered antiferromagnet
435 NiPS₃. *Journal of Physics: Condensed Matter* 6, 4569–4579. doi:10.1088/0953-8984/6/24/017
- 436 Coak, M. J., Jarvis, D. M., Hamidov, H., Haines, C. R. S., Alireza, P. L., Liu, C., et al. (2020).
437 Tuning dimensionality in van-der-Waals antiferromagnetic Mott insulators TMPS₃. *Journal of Physics:
438 Condensed Matter* 32, 124003. doi:10.1088/1361-648X/ab5be8
- 439 Coak, M. J., Jarvis, D. M., Hamidov, H., Wildes, A. R., Paddison, J. A. M., Liu, C., et al. (2021). Emergent
440 Magnetic Phases in Pressure-Tuned van der Waals Antiferromagnet FePS₃. *Physical Review X* 11,
441 011024. doi:10.1103/PhysRevX.11.011024

- 442 Coak, M. J., Son, S., Daisenberger, D., Hamidov, H., Haines, C. R. S., Alireza, P. L., et al. (2019).
443 Isostructural Mott transition in 2D honeycomb antiferromagnet $V_{0.9}PS_3$. *npj Quantum Materials* 4, 38.
444 doi:10.1038/s41535-019-0178-8
- 445 Cui, H., Yun, S., Lee, K. J., Lee, C., Chang, S. H., Lee, Y., et al. (2021). Quasihydrostatic versus
446 nonhydrostatic pressure effects on the electrical properties of $NiPS_3$. *Physical Review Materials* 5,
447 124008. doi:10.1103/PhysRevMaterials.5.124008
- 448 Dedkov, Y., Guo, Y., and Voloshina, E. (2023). enProgress in the studies of electronic and magnetic
449 properties of layered MPX₃ materials (m: transition metal, x: chalcogen). *Electron. Struct.* 5, 043001
- 450 Deng, H., Yu, T., Du, C., Shen, R., Zhao, Y., He, X., et al. (Friction, under review, (2024)). $NiPS_3$: A
451 ternary 2D material with an ultra-low friction coefficient
- 452 Deng, S., Chen, S., Monserrat, B., Artacho, E., and Saxena, S. S. (2023). Pressure-induced transitions in
453 $FePS_3$: Structural, magnetic and electronic properties. *SciPost Phys.* 15, 020. doi:10.21468/SciPostPhys.
454 15.1.020
- 455 Friedel, M. C. (1894). Sur une nouvelle série de sulfophosphures, les thiohypophosphates. *Comptes rendus*
456 *de l'Académie des Sciences* 119, 260–264
- 457 Fujii, M., Yamaguchi, T., Ohkochi, T., De, C., Cheong, S.-W., and Mizokawa, T. (2022). Bulk and surface
458 electronic structure of $mnpse_3$ revealed by photoemission and x-ray absorption spectroscopy. *Phys. Rev.*
459 *B* 106, 035118. doi:10.1103/PhysRevB.106.035118
- 460 Grasso, V., Neri, F., Perillo, P., Silipigni, L., and Piacentini, M. (1991). Optical-absorption spectra of
461 crystal-field transitions in mnp_s_3 at low temperatures. *Phys. Rev. B* 44, 11060–11066. doi:10.1103/
462 PhysRevB.44.11060
- 463 Gu, Y., Zhang, S., and Zou, X. (2021). Tunable magnetism in layered $CoPS_3$ by pressure and carrier
464 doping. *Science China Materials* 64, 673–682. doi:10.1007/s40843-020-1453-0
- 465 Haines, C. R. S., Coak, M. J., Wildes, A. R., Lampronti, G. I., Liu, C., Nahai-Williamson, P., et al. (2018).
466 Pressure-Induced Electronic and Structural Phase Evolution in the van der Waals Compound $FePS_3$.
467 *Physical Review Letters* 121, 266801. doi:10.1103/PhysRevLett.121.266801
- 468 Harms, N. C., Kim, H.-s., Clune, A. J., Smith, K. A., O'Neal, K. R., Haglund, A. V., et al. (2020).
469 Piezochromism in the magnetic chalcogenide $MnPS_3$. *npj Quantum Materials* 5, 56. doi:10.1038/
470 s41535-020-00259-5
- 471 Harms, N. C., Matsuoka, T., Samanta, S., Clune, A. J., Smith, K. A., Haglund, A. V., et al. (2022a).
472 Symmetry progression and possible polar metallicity in $NiPS_3$ under pressure. *npj 2D Materials and*
473 *Applications* 6, 40. doi:10.1038/s41699-022-00313-9
- 474 Harms, N. C., Smith, K. A., Haglund, A. V., Mandrus, D. G., Liu, Z., Kim, H.-s., et al. (2022b). Metal Site
475 Substitution and Role of the Dimer on Symmetry Breaking in $FePS_3$ and $CrPS_4$ under Pressure. *ACS*
476 *Applied Electronic Materials* 4, 3246–3255. doi:10.1021/acsaelm.2c00563
- 477 Hiroi, Z. (2008). A brief comment on the chemical formulae of the rare earth iron arsenide oxide
478 superconductors
- 479 Ichimura, K. and Sano, M. (1991). Electrical conductivity of layered transition-metal phosphorus trisulfide
480 crystals. *Synthetic Metals* 45, 203–211. doi:10.1016/0379-6779(91)91804-J
- 481 Jackeli, G. and Khaliullin, G. (2009). Mott insulators in the strong spin-orbit coupling limit: From
482 heisenberg to a quantum compass and kitaev models. *Phys. Rev. Lett.* 102, 017205. doi:10.1103/
483 PhysRevLett.102.017205
- 484 JOHNSON, J. W. and Jacobson, A. (1982). Intercalation chemistry of metal phosphorus trichalcogenides.
485 In *Intercalation Chemistry* (Academic Press Inc New York). 267–283

- 486 Joy, P. A. and Vasudevan, S. (1992). Magnetism in the layered transition-metal thiophosphates MPS_3 (M
487 =Mn, Fe, and Ni). *Physical Review B* 46, 5425–5433. doi:10.1103/PhysRevB.46.5425
- 488 Kang, S., Kim, K., Kim, B. H., Kim, J., Sim, K. I., Lee, J.-U., et al. (2020). Coherent many-body exciton
489 in van der Waals antiferromagnet $NiPS_3$. *Nature* 583, 785–789. doi:10.1038/s41586-020-2520-5
- 490 Kargar, F., Aytan, E., Ghosh, S., Lee, J., Gomez, M., Liu, Y., et al. (2019). Phonon and Thermal Properties
491 of Quasi-Two-Dimensional $FePS_3$ and $MnPS_3$ Antiferromagnetic Semiconductor Materials. *ACS Nano*
492 14, 2424–2435. doi:10.1021/acsnano.9b09839
- 493 Kim, C., Jeong, J., Lin, G., Park, P., Masuda, T., Asai, S., et al. (2021). Antiferromagnetic kitaev interaction
494 in $J_{\text{eff}} = 1/2$ cobalt honeycomb materials $Na_3Co_2SbO_6$ and $Na_2Co_2TeO_6$. *Journal of Physics: Condensed*
495 *Matter* 34, 045802. doi:10.1088/1361-648X/ac2644
- 496 Kim, C., Jeong, J., Park, P., Masuda, T., Asai, S., Itoh, S., et al. (2020). Spin waves in the two-
497 dimensional honeycomb lattice xxz-type van der waals antiferromagnet $CoPS_3$. *Phys. Rev. B* 102, 184429.
498 doi:10.1103/PhysRevB.102.184429
- 499 Kim, C., Kim, S., Park, P., Kim, T., Jeong, J., Ohira-Kawamura, S., et al. (2023). Bond-dependent
500 anisotropy and magnon decay in cobalt-based kitaev triangular antiferromagnet. *Nature Physics* 19,
501 1624–1629. doi:10.1038/s41567-023-02180-7
- 502 Kim, H.-S., Haule, K., and Vanderbilt, D. (2019). Mott Metal-Insulator Transitions in Pressurized Layered
503 Trichalcogenides. *Physical Review Letters* 123, 236401. doi:10.1103/PhysRevLett.123.236401
- 504 Kim, M., Kim, H.-S., Haule, K., and Vanderbilt, D. (2022). Orbital-selective mott phase and non-fermi
505 liquid in $FePS_3$. *Phys. Rev. B* 105, L041108. doi:10.1103/PhysRevB.105.L041108
- 506 Kim, S. Y., Kim, T. Y., Sandilands, L. J., Sinn, S., Lee, M. C., Son, J., et al. (2018). Charge-Spin
507 Correlation in van der Waals Antiferromagnet $NiPS_3$. *Physical Review Letters* 120, 136402. doi:10.
508 1103/PhysRevLett.120.136402
- 509 Kitaev, A. (2006). Anyons in an exactly solved model and beyond. *Annals of Physics* 321, 2–111.
510 doi:https://doi.org/10.1016/j.aop.2005.10.005. January Special Issue
- 511 Klingen, W., Ott, R., and Hahn, H. (1973). Über die darstellung und eigenschaften von hexathio-und
512 hexaselenohypodiphosphaten. *Zeitschrift für anorganische und allgemeine Chemie* 396, 271–278
- 513 Kuntu, D. V., Arkhipova, E. A., Shelukhin, L. A., Mertens, F., Prosnikov, M. A., Eliseyev, I. A., et al.
514 (2023). Laser-induced Demagnetization in van der Waals XY - and Ising-like Antiferromagnets $NiPS_3$
515 and $FePS_3$, 1–12
- 516 Kurosawa, K., Saito, S., and Yamaguchi, Y. (1983a). Neutron Diffraction Study on $MnPS_3$ and $FePS_3$.
517 *Journal of the Physical Society of Japan* 52, 3919–3926. doi:10.1143/JPSJ.52.3919
- 518 Kurosawa, K., Saito, S., and Yamaguchi, Y. (1983b). Neutron diffraction study on $MnPS_3$ and $FePS_3$.
519 *Journal of the Physical Society of Japan* 52, 3919–3926. doi:10.1143/JPSJ.52.3919
- 520 Lançon, D., Walker, H. C., Ressouche, E., Ouladdiaf, B., Rule, K. C., McIntyre, G. J., et al. (2016).
521 Magnetic structure and magnon dynamics of the quasi-two-dimensional antiferromagnet $FePS_3$. *Physical*
522 *Review B* 94, 214407. doi:10.1103/PhysRevB.94.214407
- 523 Lane, C. and Zhu, J.-X. (2020). Thickness dependence of electronic structure and optical properties
524 of a correlated van der Waals antiferromagnetic $NiPS_3$ thin film. *Physical Review B* 102, 075124.
525 doi:10.1103/PhysRevB.102.075124
- 526 Le Flem, G., Brec, R., Ouvard, G., Louisy, A., and Segransan, P. (1982). Magnetic interactions in the
527 layer compounds MPX_3 ($M = Mn, Fe, Ni; X = S, Se$). *Journal of Physics and Chemistry of Solids* 43,
528 455–461. doi:10.1016/0022-3697(82)90156-1
- 529 Lee, J.-U., Lee, S., Ryoo, J. H., Kang, S., Kim, T. Y., Kim, P., et al. (2016). Ising-Type Magnetic Ordering
530 in Atomically Thin $FePS_3$. *Nano Letters* 16, 7433–7438. doi:10.1021/acs.nanolett.6b03052

- 531 Lin, G., Jeong, J., Kim, C., Wang, Y., Huang, Q., Masuda, T., et al. (2021). Field-induced quantum
532 spin disordered state in spin-1/2 honeycomb magnet $\text{Na}_2\text{Co}_2\text{TeO}_6$. *Nature Communications* 12, 5559.
533 doi:10.1038/s41467-021-25567-7
- 534 Liu, B., Yang, Y., Fu, Y., and He, J. (2022). Study on Physical Properties of Two-Dimensional Layered
535 Magnetic Semiconductor Material FePSe_3 . *Advances in Condensed Matter Physics* 11, 21–27. doi:10.
536 12677/CMP.2022.112003
- 537 Liu, H. and Khaliullin, G. (2018). Pseudospin exchange interactions in d^7 cobalt compounds: Possible
538 realization of the Kitaev model. *Phys. Rev. B* 97, 014407. doi:10.1103/PhysRevB.97.014407
- 539 Ma, X., Wang, Y., Yin, Y., Yue, B., Dai, J., Cheng, J., et al. (2021). Dimensional crossover tuned by
540 pressure in layered magnetic NiPS_3 . *Science China Physics, Mechanics & Astronomy* 64, 297011.
541 doi:10.1007/s11433-021-1727-6
- 542 Mai, T. T., Garrity, K. F., McCreary, A., Argo, J., Simpson, J. R., Doan-Nguyen, V., et al. (2021). Magnon-
543 phonon hybridization in 2D antiferromagnet MnPS_3 . *Science Advances* 7, 1–7. doi:10.1126/sciadv.
544 abj3106
- 545 Matsuoka, T., Haglund, A., Xue, R., Smith, J. S., Lang, M., dos Santos, A. M., et al. (2021). Pressure-
546 induced insulator–metal transition in two-dimensional Mott insulator NiPS_3 . *Journal of the Physical
547 Society of Japan* 90, 124076. doi:10.7566/JPSJ.90.124706
- 548 Matsuoka, T., Rao, R., Susner, M. A., Conner, B. S., Zhang, D., and Mandrus, D. (2023). Pressure-induced
549 insulator-to-metal transition in the van der Waals compound CoPS_3 . *Physical Review B* 107, 165125.
550 doi:10.1103/PhysRevB.107.165125
- 551 Mehawat, K., Alfonsov, A., Selter, S., Shemerliuk, Y., Aswartham, S., Büchner, B., et al. (2022). Low-
552 energy excitations and magnetic anisotropy of the layered van der Waals antiferromagnet $\text{Ni}_2\text{P}_2\text{S}_6$.
553 *Physical Review B* 105, 214427. doi:10.1103/PhysRevB.105.214427
- 554 Momma, K. and Izumi, F. (2011). VESTA3 for three-dimensional visualization of crystal, volumetric and
555 morphology data. *Journal of Applied Crystallography* 44, 1272–1276. doi:10.1107/S0021889811038970
- 556 Musfeldt, J. L., Iwasa, Y., and Tenne, R. (2020). Nanotubes from layered transition metal dichalcogenides.
557 *Physics Today* 73, 42–48. doi:10.1063/PT.3.4547
- 558 Nauman, M., Kiem, D. H., Lee, S., Son, S., Park, J.-G., Kang, W., et al. (2021). Complete mapping of
559 magnetic anisotropy for prototype Ising van der Waals FePS_3 . *2D Materials* 8, 035011. doi:10.1088/
560 2053-1583/abed3
- 561 Neal, S. N., Kim, H.-S., O’Neal, K. R., Haglund, A. V., Smith, K. A., Mandrus, D. G., et al. (2020).
562 Symmetry crossover in layered MPS_3 complexes ($M = \text{Mn, Fe, Ni}$). *Physical Review B* 102, 085408.
563 doi:10.1103/PhysRevB.102.085408
- 564 Neal, S. N., Kim, H.-S., Smith, K. A., Haglund, A. V., Mandrus, D. G., Bechtel, H. A., et al. (2019). Near-
565 field infrared spectroscopy of monolayer MnPS_3 . *Phys. Rev. B* 100, 075428. doi:10.1103/PhysRevB.
566 100.075428
- 567 Niu, M., Cheng, H., Li, X., Yu, J., Yang, X., Gao, Y., et al. (2022). Pressure-induced phase transitions in
568 weak interlayer coupling CdPS_3 . *Applied Physics Letters* 120, 233104. doi:10.1063/5.0089478
- 569 Ouvrard, G., Brec, R., and Rouxel, J. (1982). Synthesis and physical characterization of the lamellar
570 compound CoPS_3 . *Chemischer Informationsdienst* 13, 971
- 571 Ouvrard, G., Brec, R., and Rouxel, J. (1985a). Structural determination of some MPS_3 layered phases (M
572 = Mn, Fe, Co, Ni and Cd). *Materials Research Bulletin* 20, 1181–1189. doi:10.1016/0025-5408(85)
573 90092-3

- 574 Ouvrard, G., Fréour, R., Brec, R., and Rouxel, J. (1985b). A mixed valence compound in the two
575 dimensional MPS_3 family: $V_{0.78}PS_3$ structure and physical properties. *Materials Research Bulletin* 20,
576 1053–1062. doi:10.1016/0025-5408(85)90204-1
- 577 Park, K., Mandrus, D., Kim, H. S., and Musfeldt, J. L. (2024). Unpublished work
- 578 Pei, Q., Wang, X.-C., Zou, J.-J., and Mi, W.-B. (2018). Tunable electronic structure and magnetic coupling
579 in strained two-dimensional semiconductor $MnPS_3$. *Frontiers of Physics* 13, 137105. doi:10.1007/
580 s11467-018-0796-9
- 581 Pei, S., Wang, Z., and Xia, J. (2022). High pressure studies of 2D materials and heterostructures: A review.
582 *Materials Design* 213, 110363. doi:10.1016/j.matdes.2021.110363
- 583 Ressouche, E., Loire, M., Simonet, V., Ballou, R., Stunault, A., and Wildes, A. (2010). Magnetoelectric
584 $MnPS_3$ as a candidate for ferrotoroidicity. *Physical Review B* 82, 100408. doi:10.1103/PhysRevB.82.
585 100408
- 586 Sano, R., Kato, Y., and Motome, Y. (2018). Kitaev-heisenberg hamiltonian for high-spin d^7 mott insulators.
587 *Phys. Rev. B* 97, 014408. doi:10.1103/PhysRevB.97.014408
- 588 Shannon, R. D. (1976). Revised effective ionic radii and systematic studies of interatomic distances
589 in halides and chalcogenides. *Acta Crystallographica Section A* 32, 751–767. doi:10.1107/
590 S0567739476001551
- 591 Sun, H., Qiu, L., Han, Y., Yi, E., Li, J., Huo, M., et al. (2023). Coexistence of zigzag antiferromagnetic
592 order and superconductivity in compressed $NiPS_3$. *Materials Today Physics* 36, 101188. doi:10.1016/j.
593 mtphys.2023.101188
- 594 Sun, Y. J., Tan, Q. H., Liu, X. L., Gao, Y. F., and Zhang, J. (2019). Probing the Magnetic Ordering
595 of Antiferromagnetic $MnPS_3$ by Raman Spectroscopy. *Journal of Physical Chemistry Letters* 10,
596 3087–3093. doi:10.1021/acs.jpcclett.9b00758
- 597 Tezze, D., Pereira, J. M., Asensio, Y., Ipatov, M., Calavalle, F., Casanova, F., et al. (2022). Tuning the
598 magnetic properties of $NiPS_3$ through organic-ion intercalation. *Nanoscale* 14, 1165–1173. doi:10.1039/
599 D1NR07281A
- 600 Vaclavkova, D., Delhomme, A., Faugeras, C., Potemski, M., Bogucki, A., Suffczyński, J., et al. (2020).
601 Magnetoelastic interaction in the two-dimensional magnetic material $MnPS_3$ studied by first principles
602 calculations and Raman experiments. *2D Materials* 7, 035030. doi:10.1088/2053-1583/ab93e3
- 603 Wang, F., Shifa, T. A., Yu, P., He, P., Liu, Y., Wang, F., et al. (2018a). New Frontiers on van der
604 Waals Layered Metal Phosphorous Trichalcogenides. *Advanced Functional Materials* 28, 1802151.
605 doi:10.1002/adfm.201802151
- 606 Wang, Y., Ying, J., Zhou, Z., Sun, J., Wen, T., Zhou, Y., et al. (2018b). Emergent superconductivity in an
607 iron-based honeycomb lattice initiated by pressure-driven spin-crossover. *Nature Communications* 9,
608 1914. doi:10.1038/s41467-018-04326-1
- 609 Wang, Y., Zhou, Z., Wen, T., Zhou, Y., Li, N., Han, F., et al. (2016). Pressure-Driven Cooperative
610 Spin-Crossover, Large-Volume Collapse, and Semiconductor-to-Metal Transition in Manganese(II)
611 Honeycomb Lattices. *Journal of the American Chemical Society* 138, 15751–15757. doi:10.1021/jacs.
612 6b10225
- 613 Wiedenmann, A., Rossat-Mignod, J., Louisy, A., Brec, R., and Rouxel, J. (1981). Neutron diffraction
614 study of the layered compounds $MnPS_3$ and $FePS_3$. *Solid State Communications* 40, 1067–1072.
615 doi:10.1016/0038-1098(81)90253-2
- 616 Wildes, A. R., Fåk, B., Hansen, U. B., Enderle, M., Stewart, J. R., Testa, L., et al. (2023). Spin wave
617 spectra of single crystal $CoPS_3$. *Physical Review B* 107, 054438. doi:10.1103/PhysRevB.107.054438

- 618 Wildes, A. R., Kennedy, S. J., and Hicks, T. J. (1994). True two-dimensional magnetic ordering in MnPS₃.
619 *Journal of Physics: Condensed Matter* 6, L335–L341. doi:10.1088/0953-8984/6/24/002
- 620 Wildes, A. R., Okamoto, S., and Xiao, D. (2021). Search for nonreciprocal magnons in mnps₃. *Phys. Rev.*
621 *B* 103, 024424. doi:10.1103/PhysRevB.103.024424
- 622 Wildes, A. R., Simonet, V., Ressouche, E., Ballou, R., and McIntyre, G. J. (2017). The magnetic properties
623 and structure of the quasi-two-dimensional antiferromagnet CoPS₃. *Journal of Physics: Condensed*
624 *Matter* 29, 455801. doi:10.1088/1361-648X/aa8a43
- 625 Wildes, A. R., Simonet, V., Ressouche, E., McIntyre, G. J., Avdeev, M., Suard, E., et al. (2015).
626 Magnetic structure of the quasi-two-dimensional antiferromagnet NiPS₃. *Physical Review B* 92, 224408.
627 doi:10.1103/PhysRevB.92.224408
- 628 Yamaguchi, S., Okimoto, Y., Taniguchi, H., and Tokura, Y. (1996). Spin-state transition and high-spin
629 polarons in laco₃. *Phys. Rev. B* 53, R2926–R2929. doi:10.1103/PhysRevB.53.R2926
- 630 Yan, Y., Feng, D., Zhu, J., Zhou, Q., Tian, F., Li, F., et al. (2023). Lattice and electronic structural
631 evolutions in compressed multilayer MnPS₃. *The Journal of Physical Chemistry C* 127, 17186–17193.
632 doi:10.1021/acs.jpcc.3c03501
- 633 Zhang, Q., Hwangbo, K., Wang, C., Jiang, Q., Chu, J.-H., Wen, H., et al. (2021). Observation of
634 Giant Optical Linear Dichroism in a Zigzag Antiferromagnet FePS₃. *Nano Letters* 21, 6938–6945.
635 doi:10.1021/acs.nanolett.1c02188
- 636 Zhang, X., Xu, Y., Halloran, T., Zhong, R., Broholm, C., Cava, R. J., et al. (2023). A magnetic continuum
637 in the cobalt-based honeycomb magnet baco₂(aso₄)₂. *Nature Materials* 22, 58–63. doi:10.1038/
638 s41563-022-01403-1
- 639 Zheng, Y., Jiang, X.-x., Xue, X.-x., Dai, J., and Feng, Y. (2019). Ab initio study of pressure-driven phase
640 transition in FePS₃ and FePSe₃. *Physical Review B* 100, 174102. doi:10.1103/PhysRevB.100.174102
- 641 Zobel, C., Kriener, M., Bruns, D., Baier, J., Grüninger, M., Lorenz, T., et al. (2002). Evidence for a
642 low-spin to intermediate-spin state transition in laco₃. *Phys. Rev. B* 66, 020402. doi:10.1103/PhysRevB.
643 66.020402

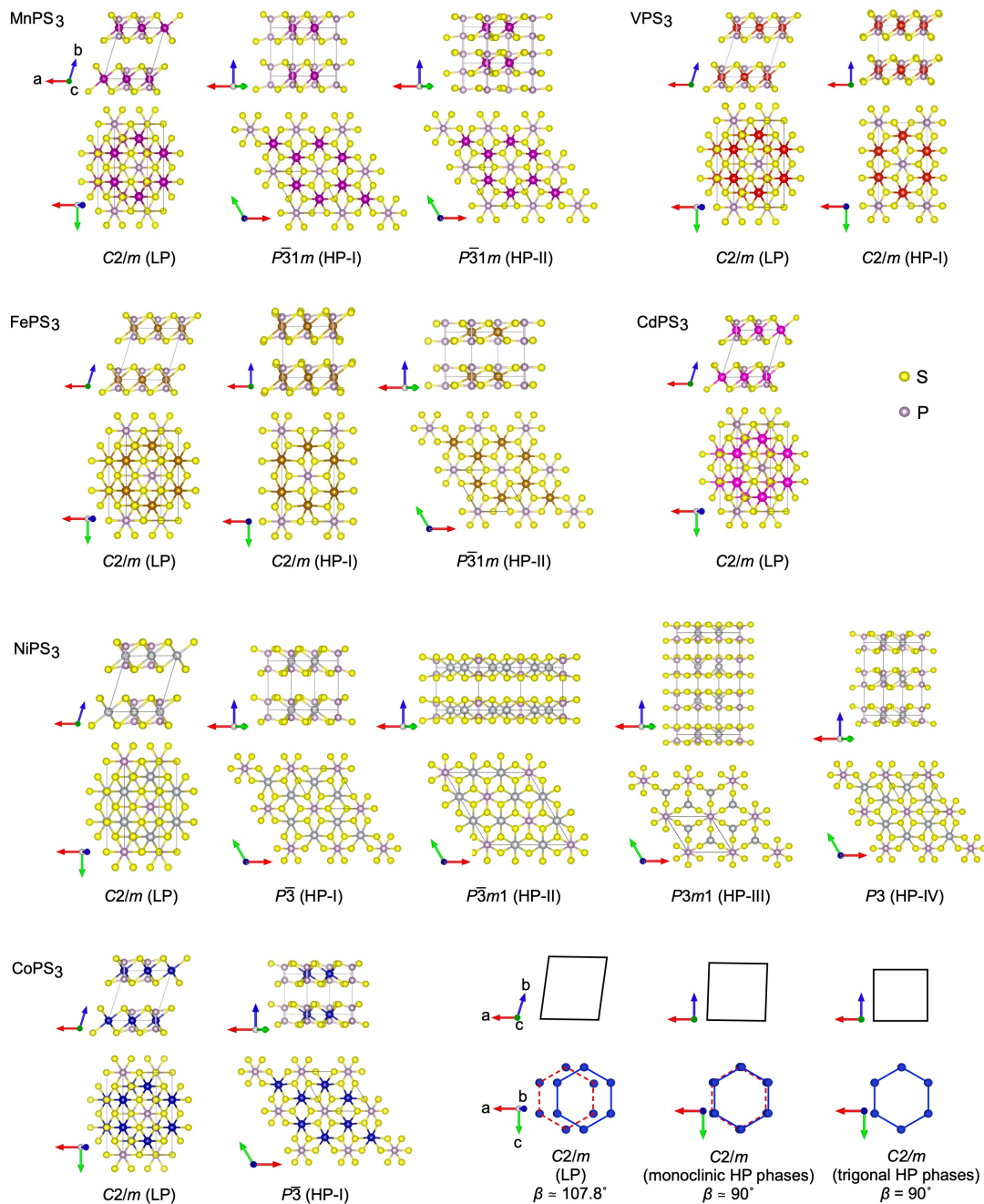


Figure 1. Crystal structures of MPS_3 ($M = V, Mn, Fe, Ni, Co, Cd$) family of materials in the low- and high-pressure phases visualized using VESTA3 (Momma and Izumi, 2011) based upon reported experimental and theoretical results. (Coak et al., 2019; Ouvrard et al., 1985a; Harms et al., 2020; Haines et al., 2018; Matsuoka et al., 2023; Harms et al., 2022a) The bottom right shows layer sliding in $C2/m$ symmetry with decreasing monoclinic angle β under pressure. When $\beta = 90^\circ$, the honeycomb pattern of metal ions overlaps between adjacent layers, and the system transforms to a trigonal high pressure phase.

FIGURE CAPTIONS

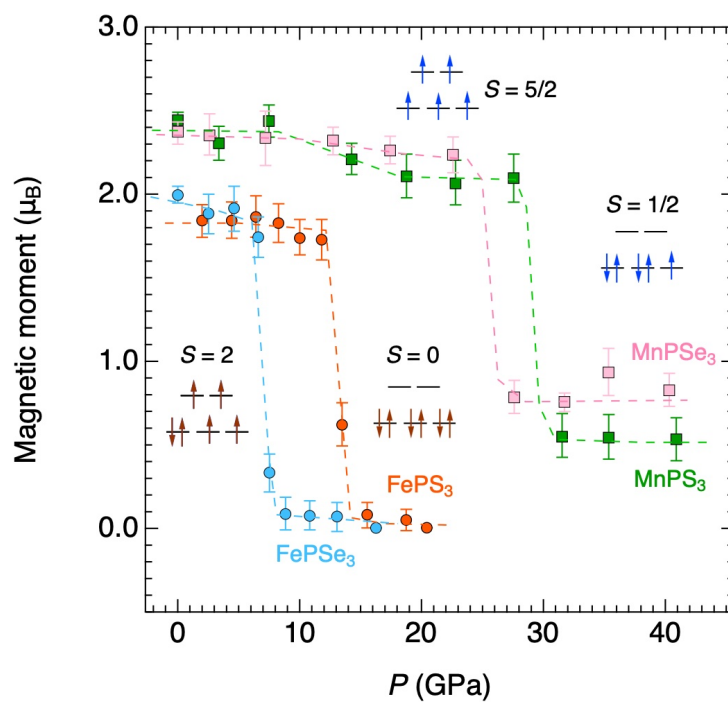


Figure 2. Magnetic moment and spin state as a function of pressure for MnPS_3 , MnPSe_3 , FePS_3 , and FePSe_3 relative to properties at ambient conditions. Data taken from (Wang et al., 2016) and (Wang et al., 2018b).

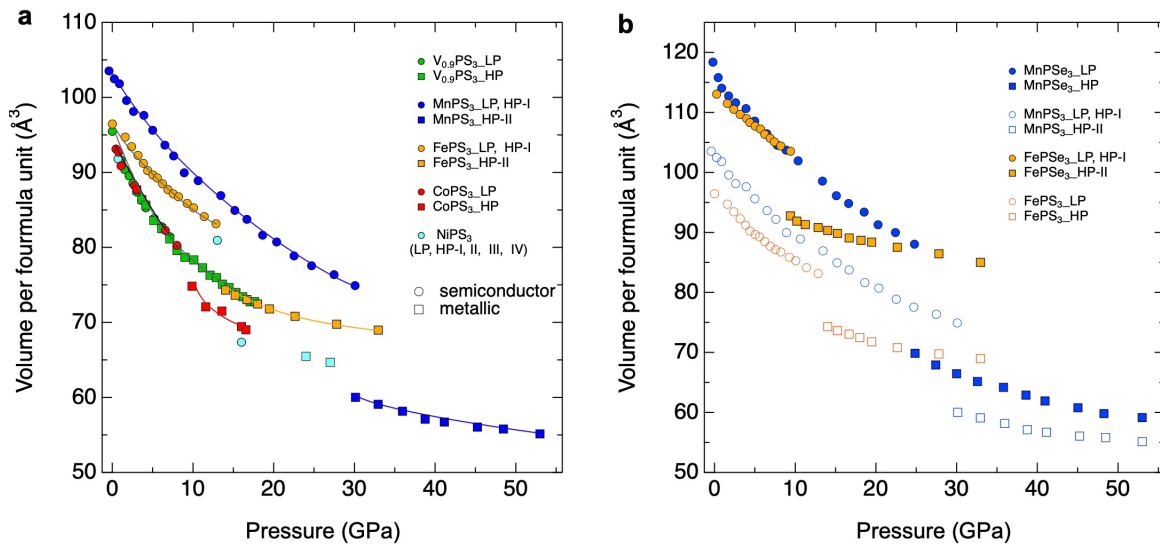


Figure 3. Volume per formula unit as a function of pressure. **(a)** MPS_3 ($M = V, Mn, Fe, Co, Ni$). **(b)** $MnPS_3$ and $FePS_3$ with $MnPSe_3$ and $FePSe_3$ for comparison. The circles denote the low (or ambient) pressure phase, which is semiconducting, including the HP-I phases for $MnPS_3$ and $FePS_3$. The squares indicate high pressure metallic phases. The solid lines guide the eyes.

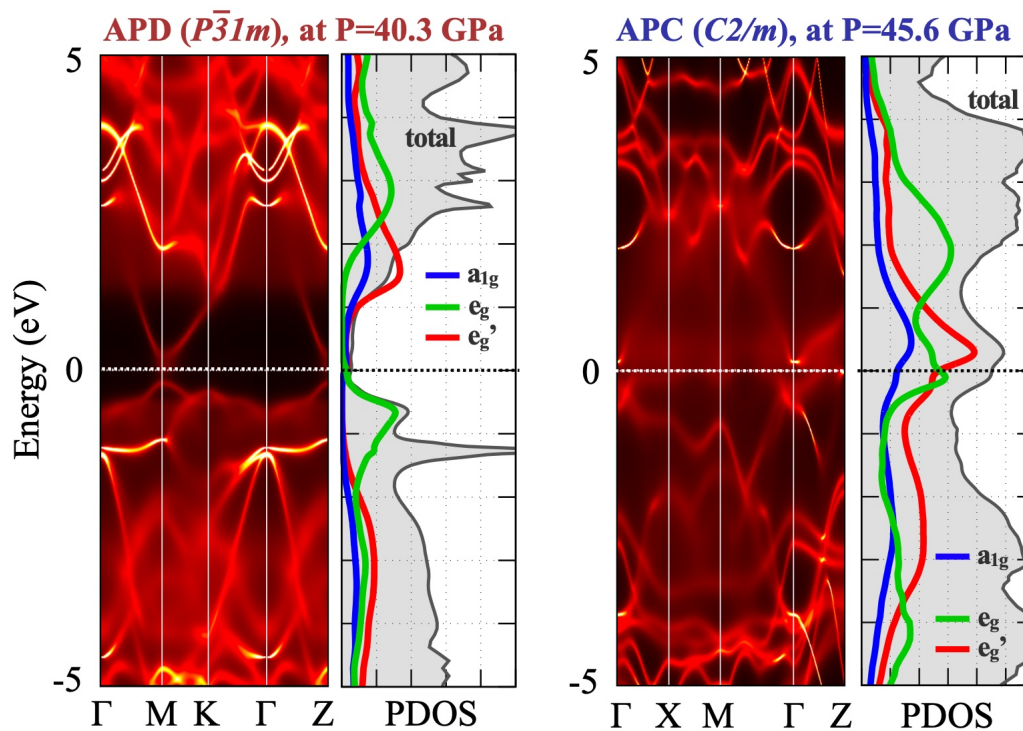


Figure 4. Spectral functions from DFT+DMFT calculations showing the k -resolved and orbital-projected spectral functions calculated with the aligned phosphorous dimer (APD) and aligned phosphorous chain (APC), respectively. (Harms et al., 2020)

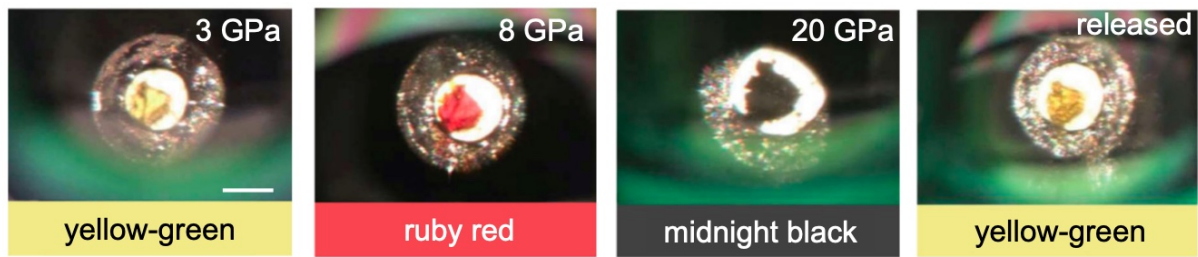


Figure 5. Photographs of piezochromic MnPS₃ inside the diamond anvil cell at several characteristic pressures and also after release at room temperature. The scale bar (left panel) is 200 μm . (Harms et al., 2020).

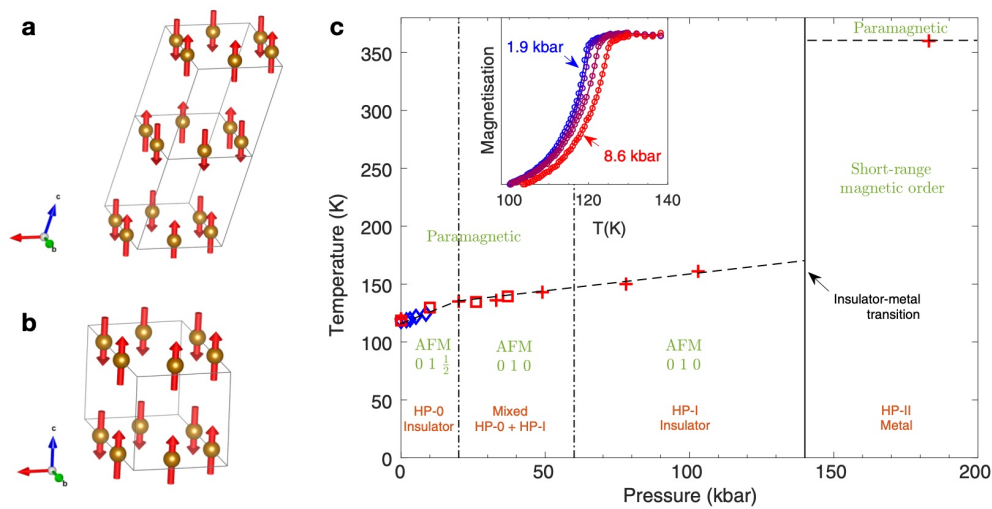


Figure 6. Crystal and magnetic structures of the ambient and the first high-pressure (HP-I) phases of FePS₃. (a) The magnetic cell of FePS₃ with the $\mathbf{k} = [0, 1, 1/2]$ propagation vector - overall antiferromagnetic order, consisting of a zig-zag chain antiferromagnetically coupled to their neighbors along a-axis and between the planes (Lançon et al., 2016). (b) The magnetic unit cell with $\mathbf{k} = [0, 1, 0]$ propagation vector, where the planes are ferromagnetically aligned (Coak et al., 2021). (c) Pressure-temperature phase diagram of FePS₃ from magnetization measurements and neutron scattering experiments. Blue circles, red crosses (and squares) are from magnetization measurements and integration of neutron spectra, respectively. Dashed lines are fits to the data points, and vertical lines mark structural transitions. Inset shows normalized magnetization versus temperature with increasing pressure. The plot is from (Coak et al., 2021).

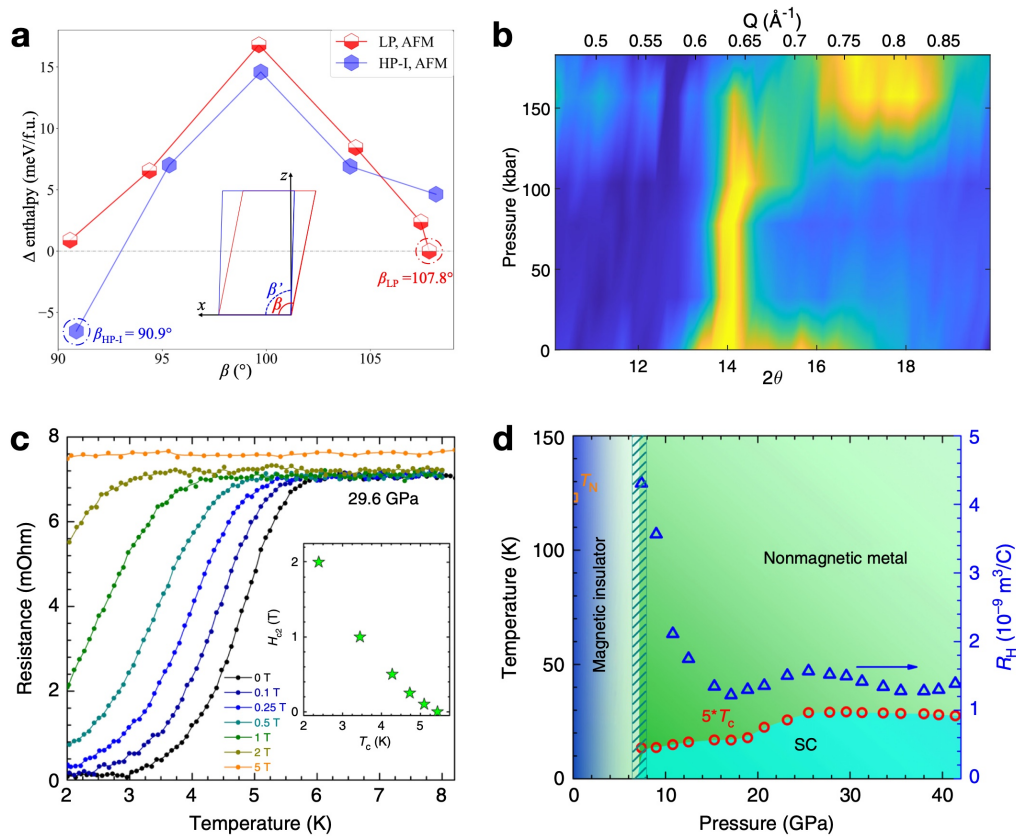


Figure 7. High-pressure electronic states of FePS₃ and superconducting FePSe₃ (a) Enthalpy difference from DFT calculations as a function of the monoclinic β angle in the $C2/m$ structure for the ambient (LP) and HP-I AFM phases of FePS₃ at 1.0 GPa. Panel from Deng et al. (2023). (b) Heat map of magnetic peaks at 80 K in FePS₃, showing the presence of magnetic signals in the HP-II ($P > 15$ GPa) phase. Panel from Coak et al. (2021). (c) The temperature dependence of the electrical resistance of FePSe₃ at 29.6 GPa under magnetic fields of 0, 0.1, 0.25, 0.5, 1, 2, and 5 T. Inset shows the field dependence of T_c for FePSe₃ at 29.6 GPa. (d) Temperature–pressure phase diagram of FePSe₃. Solid circles: the pressure dependence of the onset superconducting transition temperatures ($5 \cdot T_c$), blue triangles: the pressure dependence of Hall coefficient, T_N denoting the Néel temperature. Panel (c) and (d) from (Wang et al., 2018b).

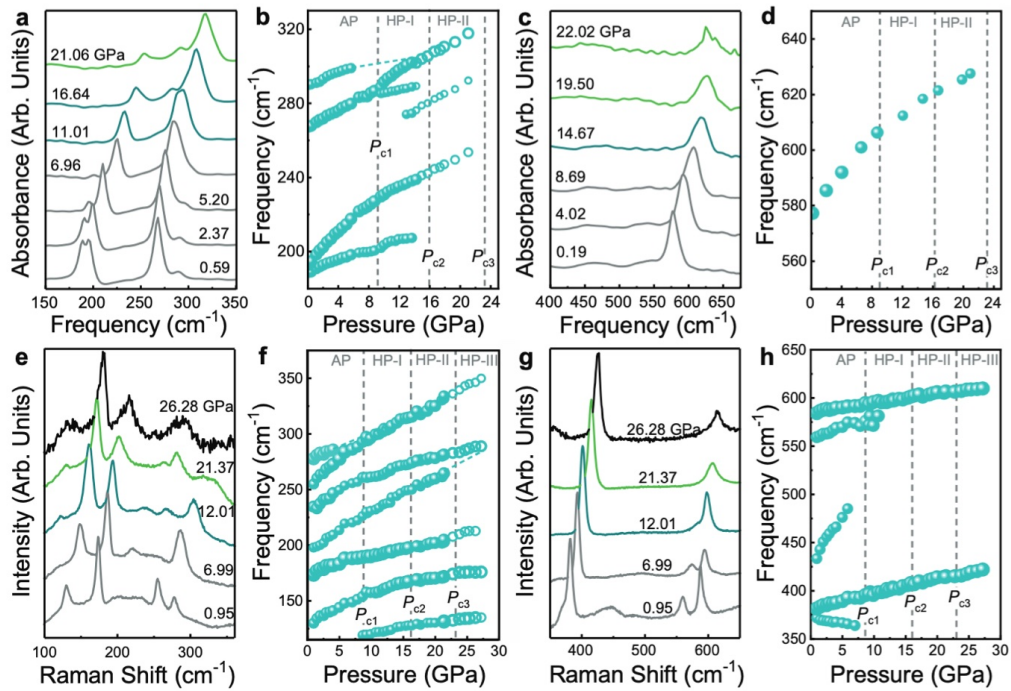


Figure 8. Vibrational properties of NiPS_3 under compression. (a-d) Close-up view of the infrared absorption and frequency vs. pressure plots. (e-h) Close-up view of the Raman scattering response and frequency vs. pressure plots. Spectra for the ambient pressure (LP) phase are shown in gray; those for the high pressure phases (HP-I, HP-II, and HP-III) are shown in teal, green, and black, respectively. Closed and open circles represent two independent runs. Note that infrared spectra in the HP-III phase are not included because the phonons are screened by the metallic response. The critical pressures (P_C 's) separate the high pressure phases and are indicated with dashed vertical gray lines. Panels (a)-(h) from (Harms et al., 2022a)

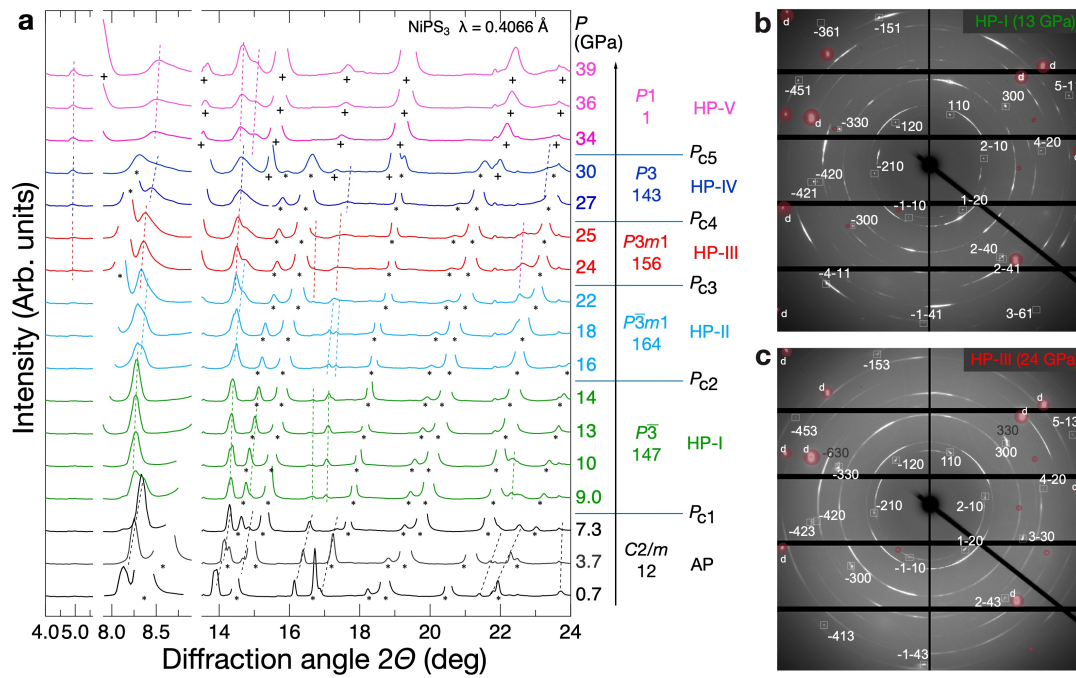


Figure 9. High pressure x-ray diffraction results of NiPS₃ up to 39 GPa. **(a)** Integrated x-ray diffraction profiles at pressures. The appearance of x-ray diffraction peaks at the given angle are indicated, alongside dashed lines to guide the eye. Critical pressures, dividing individual pressure phases, are indicated by solid blue horizontal lines. The space groups of individual high pressure phases are labeled. The asterisk (*) and plus (+) marks correspond to the diffraction response from NaCl in B1-type structure (below 30 GPa) and B2-type (above 30 GPa). **(b)** and **(c)** The x-ray diffraction images on the detector for HP-I (13 GPa) and HP-III (24 GPa). The peaks from NiPS₃ are enclosed with squares alongside the *hkl* indices for each phase. The gray labels in the panel (c) indicate the diffraction from HP-II. The Bragg diffraction from the diamond anvils is masked with red circles. Panels (a-c) from (Harms et al., 2022a)

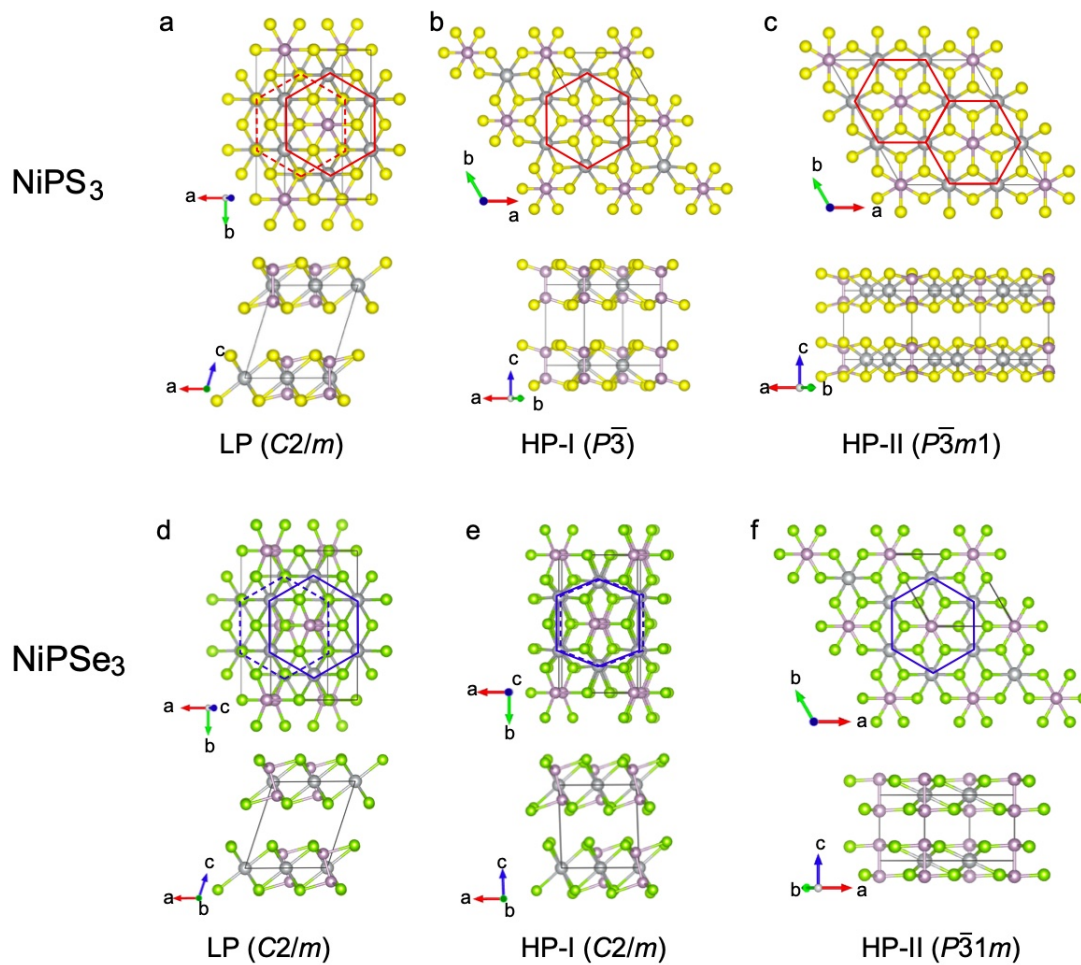


Figure 10. Crystal structures of NiPS_3 and NiPSe_3 in LP ((a) and (d)), HP-I ((b) and (e)), and HP-II ((c) and (f)) phases visualized using VESTA3 (Momma and Izumi, 2011) based on the experimental reports (Harms et al., 2022a; Sun et al., 2023). As discussed in the text, NiPS_3 displays an unusual sequence under pressure: $C2/m$ with $\beta \sim 108^\circ \rightarrow P\bar{3} \rightarrow P\bar{3}m1 \rightarrow P31m$ and so on. This structural sequence is not seen in other members of the MPS_3 family. On the other hand, NiPSe_3 is similar to FePS_3 ($C2/m$ with $\beta \sim 108^\circ \rightarrow C2/m$ with $\beta \sim 90^\circ \rightarrow P\bar{3}1m$) and MnPS_3 ($C2/m$ with $\beta \sim 108^\circ \rightarrow P\bar{3}1m$). The primary difference between the LP-phases of NiPS_3 and NiPSe_3 is the angle of the P-P dimer. The P-P dimer in NiPS_3 aligns almost perpendicular to the ab plane. On the other hand, the dimer in NiPSe_3 aligns mostly in an out-of-plane direction but with an angle.

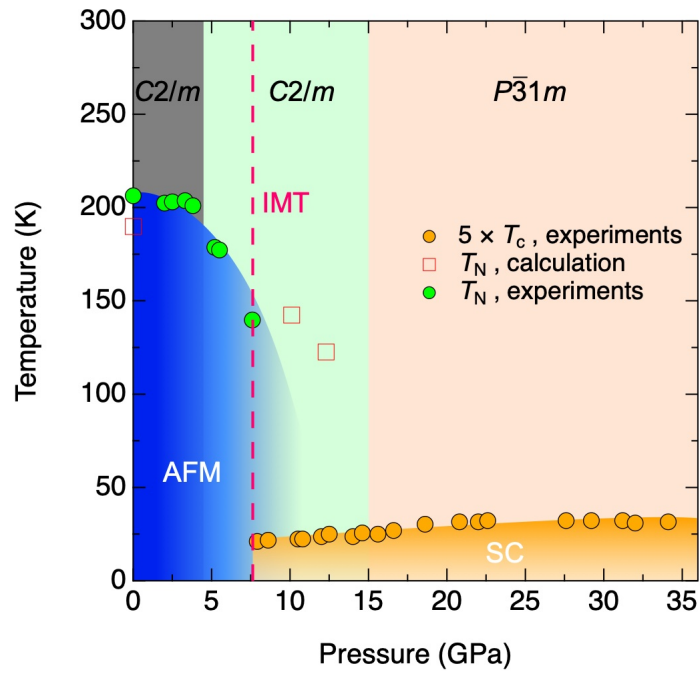


Figure 11. Phase diagram of NiPSe₃ under pressure. The insets illustrate the magnetic structures, i.e. zigzag-out for the LP phase and zigzag-in for the HP-I phase. T_N for AFM order and T_C for superconductivity are extracted from resistance measurements and DFT calculations. Created based on data from (Sun et al., 2023).

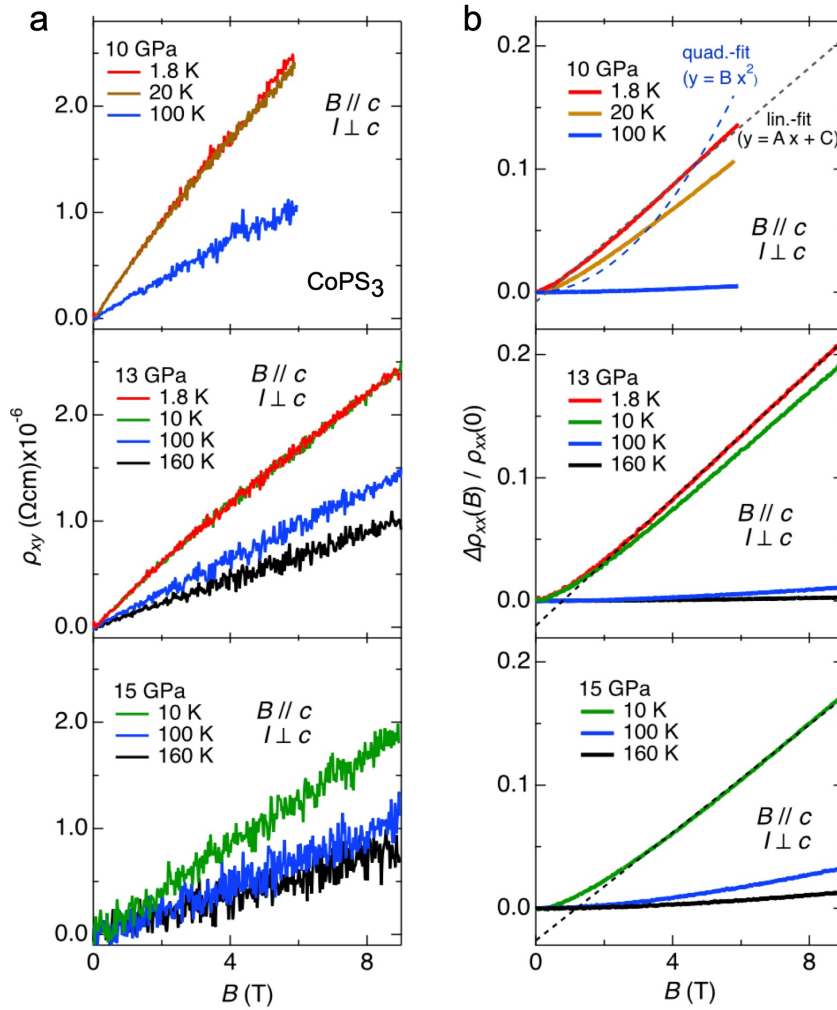


Figure 12. Transverse magnetotransport data from metallic CoPS₃. (a) The ρ_{xy} at different temperatures. The data at 1.8 K and 20 K at 10 GPa overlap (top panel). The data at 1.8 K and 10 K at 13 GPa overlap (middle panel). (b) The magnetoresistance. The dotted (black) and dashed (blue) lines in the top panel indicate the linear fit, $y = Ax + C$ and quadratic fits $y = Bx^2$ to the data at 10 GPa and 1.8 K. (Matsuoka et al., 2023) Reprinted (Figure 5) with permission from [Matsuoka, T., Rao, R., Susner, M. A., Conner, B. S., Zhang, D., and Mandrus, D., Pressure-induced insulator-to-metal transition in the van der Waals compound CoPS₃, 107, 165125 (2023)]. Copyright (2023) by the American Physical Society.

Table 1 Inter-layer distance and van der Waals (vdw) gap of MPS_3 and $MPSe_3$. Data are from (Ouvrard et al., 1985b,a; Wiedenmann et al., 1981)

| | $V_{0.78}PS_3$ | $MnPS_3$ | $FePS_3$ | $CoPS_3$ | $NiPS_3$ | $CdPS_3$ | $MnPSe_3$ | $FePSe_3$ |
|-----------------------------|----------------|----------|----------|----------|----------|----------|-----------|-----------|
| layer thickness (Å) | 6.363 | 6.487 | 6.423 | 6.361 | 6.343 | 6.546 | 6.673 | 6.604 |
| vdw gap (Å) | 3.227 | 3.247 | 3.250 | 3.243 | 3.258 | 3.218 | 3.275 | 3.174 |
| (layer thickness)/(vdW gap) | 0.507 | 0.500 | 0.506 | 0.510 | 0.514 | 0.492 | 0.491 | 0.481 |

Table 2 Crystal structures for the ambient pressure (AP) and high pressure (HP) phases of MPS_3 .

| | P (GPa) | Phase | Symmetry | Lattice constants | Ref. |
|---------------|-----------|-------|--------------|--|-------------------------|
| $V_{0.9}PS_3$ | 1.1 | AP | $C2/m$ | $a = 5.8436(15) \text{ \AA}$ $b = 10.0876(8) \text{ \AA}$ $c = 6.5237(18) \text{ \AA}$ $\alpha = \gamma = 90^\circ, \beta = 107.098(5)^\circ$ | (Coak et al., 2019) |
| | 1.1 | HP-I | $C2/m$ | $a = 5.5469(3) \text{ \AA}$ $b = 9.5892(6) \text{ \AA}$ $c = 5.4788(9) \text{ \AA}$ $\alpha = \gamma = 90^\circ, \beta = 90.136(8)^\circ$ | (Coak et al., 2019) |
| $MnPS_3$ | 0 | AP | $C2/m$ | $a = 6.077(1) \text{ \AA}$, $b = 10.524(3) \text{ \AA}$ $c = 6.796(1) \text{ \AA}$ $\alpha = \gamma = 90^\circ, \beta = 107.35(2)^\circ$ | (Ouvrard et al., 1985a) |
| | | HP-I | $P\bar{3}1m$ | $a = b = 5.725 \text{ \AA}$ $c = 5.758 \text{ \AA}$ $\alpha = \beta = 90^\circ, \gamma = 120^\circ$ | (Harms et al., 2020) |
| | 33 | HP-II | $C2/m$ | $a = 4.858(3) \text{ \AA}$ $b = 8.171(5) \text{ \AA}$ $c = 6.263(3) \text{ \AA}$ $\alpha = \beta = 90^\circ, \gamma = 107.98^\circ$ | (Wang et al., 2016) |
| $FePS_3$ | 0 | AP | $C2/m$ | $a = 5.9428(9) \text{ \AA}$ $b = 10.299(2) \text{ \AA}$ $c = 6.716(2) \text{ \AA}$ $\alpha = \gamma = 90^\circ, \beta = 107.34(2)^\circ$ | (Haines et al., 2018) |
| | 10 | HP-I | $C2/m$ | $a = 5.7620(12) \text{ \AA}$ $b = 9.988(2) \text{ \AA}$ $c = 5.803(5) \text{ \AA}$ $\alpha = \beta = 90^\circ, \gamma = 89.33(2)^\circ$ | (Haines et al., 2018) |
| | 18 | HP-II | $P\bar{3}m1$ | $a = b = 5.699(4) \text{ \AA}$ $c = 4.818(3) \text{ \AA}$ $\alpha = \beta = 90^\circ, \gamma = 120^\circ$ | (Haines et al., 2018) |
| $CoPS_3$ | 0.5 | AP | $C2/m$ | $a = 5.844(1) \text{ \AA}$ $b = 10.127(1) \text{ \AA}$ $c = 6.562(4) \text{ \AA}$ $\alpha = \beta = 90^\circ, \gamma = 107.04(2)^\circ$ | (Matsuoka et al., 2023) |
| | 17 | HP-I | $P\bar{3}$ | $a = b = 5.570(5) \text{ \AA}$ $c = 5.13(2) \text{ \AA}$ $\alpha = \beta = 90^\circ, \gamma = 120^\circ$ | (Matsuoka et al., 2023) |
| $NiPS_3$ | 0.7 | AP | $C2/m$ | $a = 5.800(1) \text{ \AA}$ $b = 10.057(1) \text{ \AA}$ $c = 6.605(2) \text{ \AA}$ $\alpha = \gamma = 90^\circ, \beta = 106.99(2)^\circ$ | (Harms et al., 2022a) |
| | 13 | HP-I | $P\bar{3}$ | $a = b = 5.638(5) \text{ \AA}$ | |

| | | | | | |
|-------------------|--------|--------------|--------|---|-------------------------|
| | | | | $c = 5.88(2) \text{ \AA}$ | |
| | | | | $\alpha = \beta = 90^\circ, \gamma = 120^\circ$ | |
| 16 | HP-II | $P\bar{3}m1$ | | $a = b = 9.720(1) \text{ \AA}$ | |
| | | | | $c = 4.94(1) \text{ \AA}$ | |
| 24 | HP-III | $P3m1$ | | $\alpha = \beta = 90^\circ, \gamma = 120^\circ$ | |
| | | | | $a = b = 5.582(3) \text{ \AA}$ | |
| | | | | $c = 15.03(2) \text{ \AA}$ | |
| 27 | HP-IV | $P3$ | | $\alpha = \beta = 90^\circ, \gamma = 120^\circ$ | |
| | | | | $a = b = 5.488(1) \text{ \AA}$ | |
| | | | | $c = 9.92(4) \text{ \AA}$ | |
| | | | | $\alpha = \beta = 90^\circ, \gamma = 120^\circ$ | |
| CdPS ₃ | 0 | AP | $C2/m$ | $a = 6.218(1) \text{ \AA}$ | (Ouvrard et al., 1985a) |
| | | | | $b = 10.763(2) \text{ \AA}$ | |
| | | | | $c = 6.867(1) \text{ \AA}$ | |
| | | | | $\alpha = \gamma = 90^\circ, \beta = 107.58(1)^\circ$ | |

Table 3 Crystal structures for the ambient pressure (AP) and high pressure (HP) phases of $M\text{PSe}_3$.

| | P (GPa) | Phase | Symmetry | Lattice constants | Ref. |
|------------------|-----------|-------|--------------|--|---|
| MnPSe_3 | 0 | AP | $R\bar{3}$ | $a = b = 6.387(2)\text{Å}$ $c = 19.996(6)\text{Å}$ $\alpha = \beta = 90^\circ, \gamma = 120^\circ$ | (Wiedenmann et al., 1981) |
| | 27 | HP-I | $C2/m$ | $a = 5.266(3)\text{Å}$ $b = 7.600(5)\text{Å}$ $c = 7.151(3)\text{Å}$ $\alpha = \gamma = 90^\circ, \beta = 108.17^\circ$ | (Wang et al., 2016) |
| FePSe_3 | 0 | LP | $R\bar{3}$ | $a = b = 6.262(3)\text{Å}$ $c = 6.716(2)\text{Å}$ $\alpha = \beta = 90^\circ, \gamma = 120^\circ$ | (Wiedenmann et al., 1981) (Liu et al., 2022) |
| | 18 | HP-I | $R\bar{3}$ | $a = b = 5.824\text{Å}$, $c = 19.330\text{Å}$, $\alpha = \beta = 90^\circ, \gamma = 120^\circ$ | (Wang et al., 2018b) |
| NiPSe_3 | 2.2 | AP | $C2/m$ | $a = 6.052(1)\text{Å}$ $b = 10.440(1)\text{Å}$ $c = 6.705(1)\text{Å}$ $\alpha = \gamma = 90^\circ, \beta = 108.45(2)^\circ$ | (Sun et al., 2023) |
| | 6.3 | HP-I | $C2/m$ | $a = 5.898(1)\text{Å}$ $b = 10.348(1)\text{Å}$ $c = 6.303(1)\text{Å}$ $\alpha = \gamma = 90^\circ, \beta = 88.38(1)^\circ$ | (Sun et al., 2023) |
| | 25.7 | HP-II | $P\bar{3}1m$ | $a = b = 5.873(2)\text{Å}$ $c = 4.274(4)\text{Å}$ $\alpha = \beta = 90^\circ, \gamma = 120^\circ$ | (Sun et al., 2023) |